

The Pennsylvania State University  
The Graduate School  
Department of Engineering Science and Mechanics

**INTEGRAL TIME-OF-FLIGHT AND CHARGE EXTRACTION BY LINEARLY  
INCREASING VOLTAGE TECHNIQUES FOR DETERMINING CARRIER MOBILITY**

A Thesis in  
Engineering Science  
by  
Alan Berger

Submitted in Partial Fulfillment  
of the Requirements  
for the Degree of

Master of Science

December 2009

The thesis of Alan Berger was reviewed and approved\* by the following:

Jian Xu  
Associate Professor of ESM, Adjunct Professor of EE  
Thesis Co-Advisor

S. Ashok  
Professor of Engineering Science  
Thesis Co-Advisor

Michael Lanagan  
Professor of ESM, Associate Director MRI

Albert Segall  
Professor of ESM, Graduate Officer

Judith Todd  
Professor of ESM  
P. B. Breneman Department Head for ESM

\*Signatures are on file in the Graduate School

## ABSTRACT

Charge transport properties of thin film organic solar cells are investigated using both integral time-of-flight (I-TOF) and charge extraction by linearly increasing voltage (CELIV) measurement techniques. Test devices are constructed with active layers consisting of blended of poly-3-hexylthiophene (P3HT) and [6,6]-phenyl-C61-butyric acid methyl ester (PCBM) in a glass/ITO/PEDOT:PSS/P3HT:PCBM/Al structure. Samples are tested using voltages varying from 0 to 15V and light intensities from 2.5 to 600mW. Characteristic voltage transients are obtained with each technique. From experimental data, electron mobility in the P3HT:PCBM solar cell devices is found to be on the order of  $\mu_n = 5 \times 10^{-4} \text{ cm}^2/\text{Vs}$  using I-TOF and  $\mu_n = 2 \times 10^{-5} \text{ cm}^2/\text{Vs}$  using CELIV. Both results are close to published data, with our I-TOF data being somewhere in the middle, and the CELIV results being slightly lower [1-5].

Integral TOF mobility results are probed as a function of collection capacitance, voltage, and light intensity. No significant variation is seen for changing the capacitance or the light intensity, but changing voltage yields the intriguing negative mobility dependence which has been reported in literature [6].

Comparison between the two techniques is made. The dielectric relaxation time is found to be fast while carrier lifetime is short (both relative to the transit time of carriers across the sample). These indicate redistribution of the electric field and concentration near the contact regions, a violation which will cause I-TOF measurements to be overestimated [7]. This may explain why I-TOF values are higher than their CELIV counterparts.

## TABLE OF CONTENTS

LIST OF FIGURES.....	v
LIST OF TABLES .....	vi
ACKNOWLEDGEMENTS .....	vii
Chapter 1 Introduction.....	1
1.1. Objectives.....	3
1.2. Design Requirements .....	4
Chapter 2 Literature Review .....	5
2.1. Nanoparticles .....	5
2.1.1. Nanocrystals.....	5
2.1.2. Nanorods .....	11
2.1.3. Unique Nanoparticles .....	16
2.2. Time of Flight (TOF) .....	24
2.2.1. Current Mode TOF.....	24
2.2.2. Integral Time-of-Flight (I-TOF) Theory .....	26
2.2.3. Integral Mode TOF Experiments .....	32
2.3. Charge Extraction by Linearly Increasing Voltage (CELIV).....	33
2.3.1. CELIV theory.....	34
2.3.2. CELIV Experiments.....	37
Chapter 3 Experimental Details.....	38
3.1. P3HT:PCBM Device Structure .....	38
3.2. I-TOF Experimental Setup .....	40
3.3. CELIV Experimental Setup .....	41
Chapter 4 Integral TOF Results.....	43
Chapter 5 CELIV Results.....	48
Chapter 6 Discussion.....	51
6.1. Capacitance independence of mobility.....	52
6.2. Negative voltage dependence of mobility .....	52
6.3. Intensity dependence of mobility .....	53
6.4. Comparison of I-TOF and CELIV .....	54
Chapter 7 Conclusions.....	57
7.1. Summary of accomplished work .....	57
7.2. Description of future work .....	57
References .....	59

## LIST OF FIGURES

Figure 1: Schematic diagram for a polymer-based solar cell.....	4
Figure 2: IR PbSe QD absorption and photocurrent.....	6
Figure 3: Band edges for MEH-PPV, P3HT, and PbSe NCs.....	7
Figure 4: J-V Characteristics for PbSe solar cells .....	8
Figure 5: Annealing of PbS films .....	9
Figure 6: Imaging of hyperbranched PbSe nanowires .....	12
Figure 7: Morphology of MEH-PPV:CdS films with different solvents .....	13
Figure 8: Band edges for $\text{CdSe}_x\text{Te}_{1-x}$ tetrapod nanocrystals, electrodes, and MEH-PPV .....	18
Figure 9: Hyperbranched nanoparticles .....	19
Figure 10: CdSe hyperbranched nanocrystal morphology and performance.....	20
Figure 11: CuS nanoparticles attached to MWCNTs.....	23
Figure 12: TOF transients for non-dispersive and dispersive transport.....	25
Figure 13: Effect of RC decay on TOF measurements .....	27
Figure 14: I-TOF theoretical derivation schematic.....	29
Figure 15: Circuit Schematic for Integral mode Time-of-Flight .....	32
Figure 16: Theoretical applied and output voltage signals for CELIV .....	35
Figure 17: Circuit schematic for CELIV experiments .....	37
Figure 18: Schematic of P3HT:PCBM test device .....	38
Figure 19: Band diagram for P3HT:PCBM .....	39
Figure 20: Integral TOF – literature voltage transients.....	43
Figure 21: Integral TOF – experimental voltage transient.....	44
Figure 22: Integral TOF – voltage transients for several different applied voltages .....	46
Figure 23: Integral TOF – mobility dependence on electric field.....	47
Figure 24: Integral TOF – mobility dependence on light intensity.....	47
Figure 25: Photo-CELIV – sample voltage signal .....	48
Figure 26: CELIV – voltage signals from samples tested at Asbury lab .....	49
Figure 27: Photo-CELIV – voltage signals from samples tested at Asbury lab .....	50
Figure 28: Comparison of P3HT:PCBM mobility results to accepted literature values.....	51
Figure 29: Collected charge vs. applied voltage for $\mu\text{c-Si:H}$ .....	54

## LIST OF TABLES

Table 1: Articles on “Organic Solar Cells” published online .....	1
Table 2: Effect of annealing on device properties for P3HT:ZnO.....	10
Table 3: Device properties for MEH-PPV:CdS solar cells with different solvents .....	14
Table 4: Device parameters for varying compositions of $\text{CdSe}_x\text{Te}_{1-x}$ .....	17
Table 5: Effect of NC loading on PCE for CdSe:MEH-PPV.....	17
Table 6: Integral TOF – dependence of mobility on collection capacitance .....	45
Table 7: Photo-CELIV – mobility values .....	49
Table 8: CELIV – mobility values from samples tested at Asbury lab .....	50
Table 9: Photo-CELIV – mobility values from samples tested at Asbury lab.....	50

## ACKNOWLEDGEMENTS

The author gratefully acknowledges the following individuals for their support. Advisors Dr. Xu and Dr. Ashok provided invaluable guidance throughout the project. Dr. Lanagan volunteered to sit on the thesis committee and provided numerous helpful comments, revisions, and suggestions for future work. Members of the Xu lab offered advice, suggestions, and in some cases, help taking experimental data. Most notable among these were Aaron Todd, Chunfeng Zhang, Fan Zhang, and Ting Zhu.

Furthermore, this research was significantly impacted by collaboration with the lab of Dr. John Asbury. Professor Asbury and his students Kyle Banyas, Kwang Seob Jeong, and Ryan Pensack offered their laboratory equipment and their insights on performing CELIV measurements. Their assistance went a long way in corroborating the results of the experiments presented herein.

## Chapter 1

### Introduction

Despite recent economic struggles, research in organic photovoltaics has not lost much steam. A quick search of an online database will show hundreds of articles being published in this field annually. For example, EngineeringVillage.org searches both the Compendex and Inspec databases for articles published in engineering and science related fields. Searching this combined repository yields hundreds of articles per year with the keywords “organic solar cell,” and the number has grown steadily since 2000 (see Table 1). Undoubtedly, organic solar cells are still a hot topic.

**Table 1: Articles on “Organic Solar Cells” published online**

Year	Publications
2008	1116
2007	842
2006	795
2005	633
2004	557
2003	299
2002	299
2001	200
2000	177

There is a reason for this growth. One contributing factor is recent emphasis on renewable energy. Governments and private companies have started to make investments in alternative fuels and energy production schemes. BP Solar has invested US\$500 million in a grant to U.C. Berkeley for biofuels research [8]. Global solar cell production has grown at a steady 25% annually for the past 20 years, reaching US\$9 billion in 2005 and accounting for over 1 GW/year [9]. Consumers and investors are spending money on renewable energy.



Among renewable technologies, nanocomposite solar cells hold particular promise for a number of reasons. First, they have all the advantages of a polymer. They are lightweight and flexible whereas traditional semiconductors are rigid, for the most part. In theory, organic solar cells can be grown on flexible substrates. These flexible solar cells could be incorporated into fabrics for portable applications [10]. Additionally, these polymers are synthesized and processed under much less demanding conditions than crystalline silicon. This results in an energy and cost savings [11].

Adding nanoparticles to the polymer has several benefits. The plastic can transport holes well, while the nanoparticles can be designed to enhance electron transport. In addition, the polymer matrix absorbs light strongly in the visible range, but approximately 30% of the power from solar radiation lies in the near IR spectrum [9]. The optical and electrical properties of nanoparticles are determined by their size and shape [12], and thus they can be tuned to absorb light in this frequency range. Furthermore, these nanoparticles act as multiplication centers. Typically, an incoming photon can be absorbed by an electron, excite it across the band gap, and produce an electron-hole pair. The electron and hole are then separated and driven toward the contacts to be collected for use in an outside electrical circuit. Thus, only one electron can possibly be excited and collected for a single photon. However, nanoparticles have the unique ability to produce carrier multiplication [13]. Through this process, the single photon can excite several electrons by splitting the energy of the photon between several electron-hole pairs. A group at Los Alamos National Laboratory has recorded as many as seven excitations per photon in a PbSe quantum dot using ultraviolet radiation [14]. Thus, the quantum efficiency of the device can be increased above the previous limit. For these reasons of reduced cost, increased IR utilization, and carrier multiplication, there exists strong motivation for research in nanocomposite solar cells.

### 1.1. Objectives

There are several short term objectives for this research. We would like to characterize the electrical transport in organic devices. As a device research group, we have several students whose focus is on fabrication of high quality optoelectronic devices, including the solar cells tested in this paper. Once created, the devices must then be tested to determine quality. This is the focus of the research presented in this paper. Mobility and lifetime are extremely important parameters for evaluating relative material quality. Comparing them with literature results can give vital clues to our group's progress in improving fabrication, as well as be used to investigate aspects such as radiation damage.

Over the long term, there are broader goals for this research. Ideally, the study of the transport properties in the material would lead to a greater understanding of how charge moves in the device. Currently, the transport is generally agreed to be a thermally activated hopping between localized energy states [6]. However, this knowledge does not fully describe the properties observed in the material, such as the mobility dependence on voltage and temperature. If the transport were better understood, one could tune the device for enhanced performance. In the end, the goal is to increase the efficiency of the device to a level where it can compete with other energy sources. Large area solar cells typically require a power conversion efficiency of at least 10% for viability, although lower values can be acceptable due to utility gained from the devices' flexibility [10].

For the purpose of this research, the objective is to compare two methods for determining the mobility of an organic solar cell device. Initially a composite between poly-3-hexylthiophene (P3HT) and [6,6]-phenyl-C61-butyric acid methyl ester (PCBM) will be used, but additional work will involve polymer-nanocrystal hybrids.

## 1.2. Design Requirements

One may consider the design requirements to be comprised by two parts: requirements measurement methods and requirements for the devices themselves. The methods studied should have their strengths and weaknesses evaluated based on their applicability to finding the mobility in polymer-based solar cells. Results should be reproducible. The simplicity of the technique is important as it contributes to time and cost savings; therefore, the technique should be as efficient as possible in terms of time spent and resources invested. The experiments should be able to be done with the available facilities. The procedure must be safe and non-destructive to the sample.

As for the devices, there are goals in order to reach a useful solar cell. The techniques studied in this paper should help identify and design solar cells which meet these requirements. The main requirement is a high power conversion efficiency of 10 to 15%. One might view this overarching goal as consisting of several sub-requirements, such as controlled morphology with features on the scale of the exciton diffusion length, photocarrier multiplication, and absorption tuned to the solar spectrum, among others. Other requirements include practical matters such as a long lifetime (stability against degradation), an ability to scale up manufacturing, and a low cost of production. See Figure 1 for a typical device schematic.

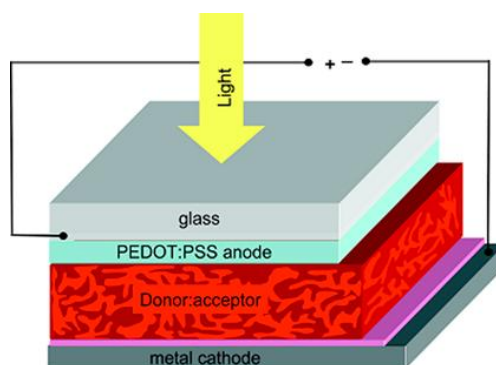


**Figure 1: Schematic diagram for a polymer-based solar cell [15]**

The area of interest is the donor:acceptor region, or the active layer. This research seeks to develop a technique for determining carrier mobility in polymer:nanocrystal active layers.

## **Chapter 2**

### **Literature Review**

In this chapter, two main topics will be covered. First, current research in nanoparticle-based solar cell devices will be highlighted. Next, an overview of techniques used to measure the mobility of charge carriers in polymer materials is provided.

#### **2.1. Nanoparticles**

One long-term goal of this research is the development of nanoparticle-based solar cells. Therefore, the purpose of this review section is two-fold. Primarily, highlighting advancements in the development of nanoparticles for solar cell applications motivates research in this area. Further, the breadth of research presented here, while certainly not all-encompassing, shows the vast potential for tailoring these devices to achieve improved performance.

##### **2.1.1. Nanocrystals**

PbSe quantum dots attract interest due to carrier multiplication, or the generation of more than one exciton for each absorbed photon. Schaller and Klimov discuss this promising feature of PbSe quantum dots [16]. They state that it occurs through impact ionization. In this process, an exciton with energy of at least  $2E_G$  ( $E_G$  is the semiconductor band gap) relaxes to a lower energy state by transferring energy of at least  $1E_G$  to an electron in the valence band. This creates two excitons from only one photon. Further, they mention that impact ionization is particularly efficient in PbSe, occurring with an  $E_G$  in the very useful near IR regime.

Another reason to use PbSe nanocrystals is that the size tunable bandgap falls within the infrared range, where much additional solar energy can be harvested that would otherwise fail to be absorbed by the conducting polymer. At University of Texas at Dallas, Dr. Jiang's group fabricates P3HT:PbSe devices [17]. ITO-coated glass with a layer of PEDOT-PSS serves as the anode. This has been the standard electrode for matching with the band edges of P3HT. Aluminum was deposited on top of the spin coated film to serve as a cathode.

To show that their dots were indeed harvesting infrared light, Jiang's group took the absorption spectra of several different diameters of their nanocrystals, which had been separated by centrifugation. The results are shown in Figure 2a. Later, the group also measured photocurrent across the spectrum, which is shown in Figure 2b. Clearly the QDs are contributing to the generation of photocurrent in the near IR spectrum. On top of this, the group also noted that under reverse bias, the photocurrent increases from  $0.2 \text{ mA/cm}^2$  to  $1 \text{ mA/cm}^2$ , so there is a potential IR photodetector application for this device.

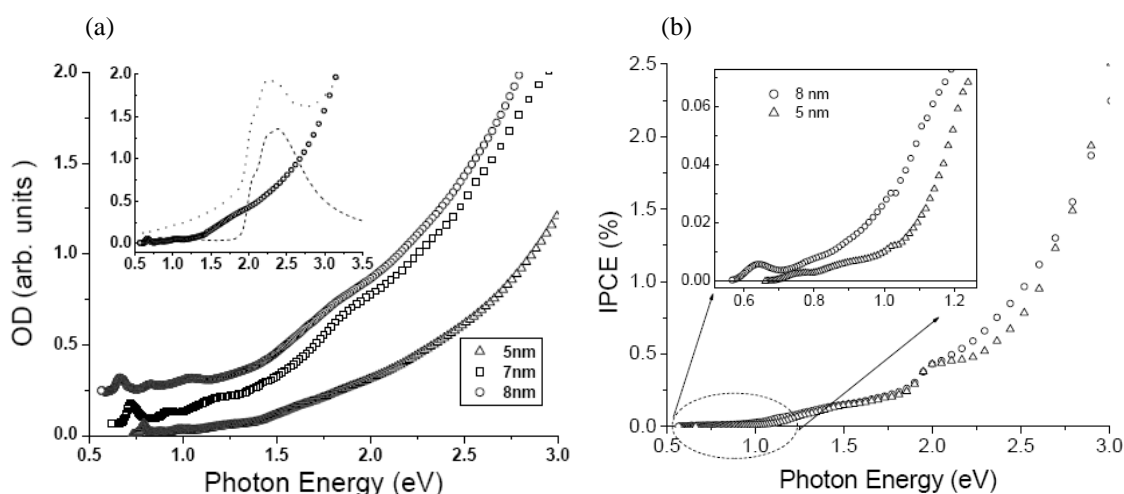


**Figure 2: IR PbSe QD absorption and photocurrent [17]**

(a) Absorption spectra of different diameter PbSe QDs in chloroform solution. Inset shows absorption spectra of QD 8 nm in solution (open circle), films of pure RRP3HT (dash line) and RRP3HT/QD 8 nm blend (dotted line). Note how QDs contribute to absorption below the P3HT cutoff. (b) Incident photon to collected electron (IPCE) efficiency for ITO/PEDOT:PSS/RR-P3HT+PbSe/Al devices with different sized PbSe dots. The inset shows that the nanoparticles contribute to photo response in the infrared region. [17]

Later, in 2007, Jiang's group produced a solar cell device using RR-P3HT and PbSe [18]. The open circuit voltage ( $V_{OC}$ ) for this device was 0.34 V, short circuit current ( $J_{SC}$ ) was 0.2 mA/cm<sup>2</sup>, and the power conversion efficiency (PCE) was 0.04% under AM1.5, 100 mW/cm<sup>2</sup>, simulated solar illumination. Lowering to 10 mW/cm<sup>2</sup> increased PCE to 0.14%. However, this research also identified an important design requirement that cannot be overlooked in solar cell design. In order for an appreciable current to flow, electrons and holes must be separated between the two media. To this extent, a type II heterojunction or "staggered gap" is preferred. This type of junction forces holes in one direction and electrons in the opposite. In general, the organic material is a good hole conductor, so we desire the conduction and valence band edges of the nanocrystals (NCs) to appear lower in energy than the HOMO and LUMO of the polymer.

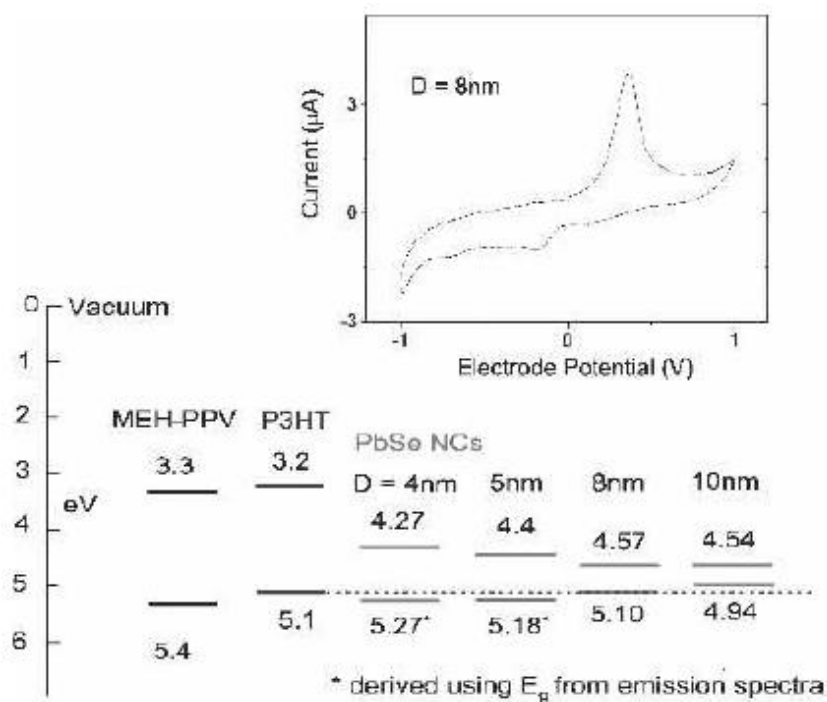


**Figure 3: Band edges for MEH-PPV, P3HT, and PbSe NCs [18]**

Energy-level positions of MEH-PPV, P3HT, and PbSe NCs of different sizes measured by electrochemical cyclic voltammetry. The dashed line traces the HOMO level of P3HT to show which sizes of NC form type II heterojunctions. Inset shows one example of a measurement with sweep rate 20 mV/s for 8 nm diameter NCs. [18]

Upon taking cyclic voltammetry measurements of their materials, Jiang's group noticed that P3HT should be preferred over MEH-PPV simply due to the type of junction it would form with the PbSe nanocrystals. This result is summarized in Figures 3 and 4. This research reiterates the importance of identifying the energy band edges in a nanocrystalline material for use in device design, bearing in mind that at this small scale, quantum effects cause the band structure to change with variations in particle size.

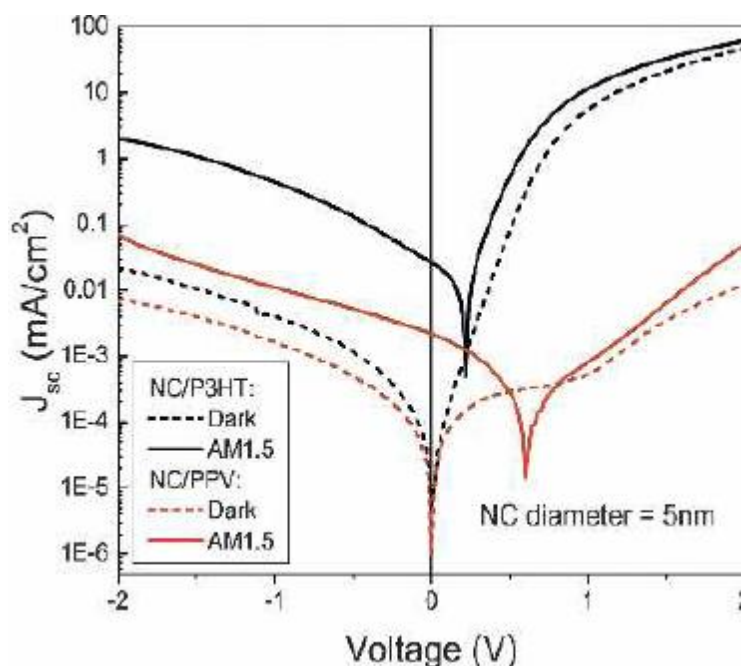


**Figure 4: J-V Characteristics for PbSe solar cells [18]**

Current–voltage characteristics are shown for dark (dashed lines) and AM1.5 illumination (solid lines). Black line shows P3HT:PbSe NC and lighter line shows MEH-PPV:PbSe NC. PbSe NCsize (EG = 0.78 eV, 5 nm NC diameter) is the same for both devices. [18]

Although many organic hybrid solar cell systems use a bulk heterojunction device structure, where the nanoparticles and polymer are spin coated from the same solution, it is still possible to create a more traditional bi-layer structure. This is exactly what a group led by Dr. Günes of the Linz Institute for Organic Solar Cells investigated [19]. They initially tried spincoating PbS nanoparticle solution from chloroform and found that agglomeration took place.

After annealing at 200°C for 1h, the particles formed a smooth layer. Following this, 1 wt% P3HT in chlorobenzene was dropcast onto the film. Unfortunately, this procedure resulted in the nanoparticles being soluble. To circumvent this problem, ethyl acetate was added into the PbS solution before casting. After annealing, the PbS film was then insoluble upon deposition of P3HT. The best device fabricated had  $J_{sc} = 0.3 \text{ mA/cm}^2$ ,  $V_{oc} = 350 \text{ mV}$  and fill factor  $FF = 0.35$ , corresponding to 0.04% PCE. To improve upon these results, the group looks to study the use of different sizes of NCs. They will also vary the surfactant used.

The annealing process was shown to have a profound impact on the morphology of this material system. The crystallization of the polymer is partly responsible for these different phases. Adding an annealing step in the fabrication of hybrid solar devices is very common, and in the case of the PbS system of Günes, the results are clearly depicted in Figure 5. This research exemplifies how critical the annealing step can be in device fabrication.

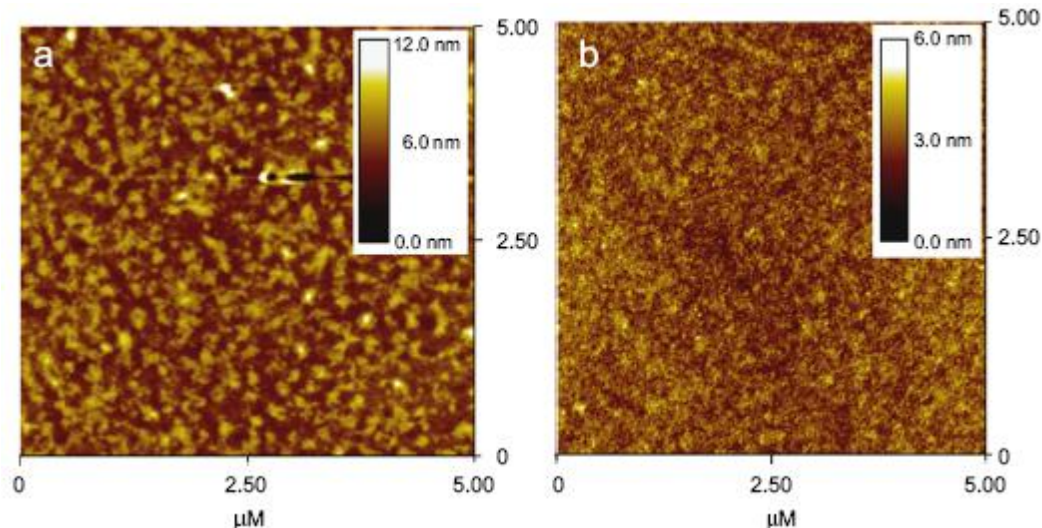


**Figure 5: Annealing of PbS films [19]**

AFM shows the morphology of PbS films both (a) before and (b) after annealing. Smoothing and breaking up of agglomerates are two of the visible benefits of this step which lead to improved device performance. [19]



A group from Eindhoven University of Technology in the Netherlands has done work on zinc oxide nanoparticles [20]. They have used both P3HT and MDMO-PPV for their conductive polymer in work that extends back to 2004. Interestingly, despite the fact that the researchers chose to move from MDMO-PPV to P3HT to take advantage of an improvement in hole mobility, the device performance actually decreased. The MDMO-PPV devices had a power conversion efficiency of about 1.6%, whereas the P3HT devices could only reach 0.9%. This decrease for nc-ZnO:P3HT devices could not be pinpointed to a single parameter; rather, each of the important device parameters ( $J_{sc}$ ,  $V_{oc}$ , and FF) all decreased by approximately 15%. Also, the maximum IPCE of 27% was less than the value of 40% found for nc-ZnO:MDMO-PPV, so the collection of charge carriers was not improved in general. One small improvement made by switching to P3HT was that the spectral response extended to 660 nm instead as opposed to only 600 nm for MDMO-PPV.

Here again, evidence for the benefits of annealing were shown. These results can be found in Table 2. Here,  $\eta$  is the overall power conversion efficiency of the device. Because the beneficial effect of annealing is greatest when the nanoparticle concentration is low, the group believes that the annealing benefits mainly the P3HT phase. Improved stacking of the P3HT chains leads to better hole transport, allowing device performance to increase.

**Table 2: Effect of annealing on device properties for P3HT:ZnO [20]**

ZnO [vol %]	$J_{sc}$ [mA cm <sup>-2</sup> ] prist./ann.	$J_{sc}$ increase [%]	$V_{oc}$ [V] prist./ann.	FF prist./ann.	Max. power [mW cm <sup>-2</sup> ] prist./ann.	$\eta$ [%] prist./ann.
8	0.36/1.18	228	0.46/0.65	0.47/0.44	0.08/0.34	0.09/0.37
15	0.90/2.20	144	0.62/0.80	0.50/0.46	0.28/0.81	0.31/0.90
26	1.71/2.19	28	0.69/0.69	0.45/0.55	0.53/0.83	0.59/0.92
35	1.52/1.70	12	0.60/0.62	0.44/0.54	0.40/0.57	0.44/0.63
42	1.54/1.81	18	0.57/0.57	0.45/0.54	0.40/0.56	0.44/0.62

### 2.1.2. Nanorods

Standard nanocrystals are not the only materials being investigated for use in hybrid solar cells. Both electrons and holes require percolation networks between cathode and anode for efficient charge collection. Meanwhile, exciton diffusion lengths are so short in these materials that domain sizes must be kept to tens of nanometers across. Domain size refers to the distance between interfaces in the active layer, and it correlates to the distance an exciton must travel before it encounters a junction and charge is separated. Here, we will discuss how several groups seek to use nanorods to fulfill these design requirements by geometric constraint.

Finlayson reports that, due to networking between rods and a reduced number of “hops” an electron must make from nanocrystal to nanocrystal, one can obtain better transport by forming rod shaped nanocrystals. These longer shapes are more likely to link together and thereby provide an easy path (minimal hopping from dot to dot) for the electron to reach the anode without recombining [21].

At Stanford, recent research has focused on the development of lead selenide nanowires (NW) for use in multi-exciton solar cell applications (among other things) [22]. These NWs were grown on Si <001> substrates with a native oxide or on NaCl <001> substrates, consistent with the PbSe rock salt structure. The research team utilized the VLS mechanism for growing NW. By incorporating a small amount of a low melting point metal catalyst into the vapor, such as In, Ga, and Bi, these nanowires formed a branching network. This branching network was investigated with SEM and TEM including SAD and EDX. EDX verified that the ratio of Pb and Se was close to 1:1. Both SEM and TEM show 90° branching for the new nucleated nanowires (Figure 6a). HRTEM showed that the nanowires were single-crystalline, and the spacing of the lattice planes parallel or perpendicular to the NW long axis was 3.06 Å, which is consistent with the (200) planes of the PbSe rock-salt structure (Figure 6d).

Further investigation at the branching interface (Figure 6c) gave the same lattice spacing and proved that the branches extending from the main NW were also single crystalline. The authors then hypothesized that the main and branched NWs belonged to the same single crystal. To test this theory, selected area electron diffraction (SAD) measurement was made at the interface of main and branched NWs (Figure 6b). The SAD showed a square lattice, consistent with diffraction patterns along the  $\langle 001 \rangle$  zone axis. The long axis of the main and branched NWs is along the same crystallographic direction of  $\langle 100 \rangle$ . As this was consistent with the HRTEM studies, the researchers were satisfied that the network was single crystalline.

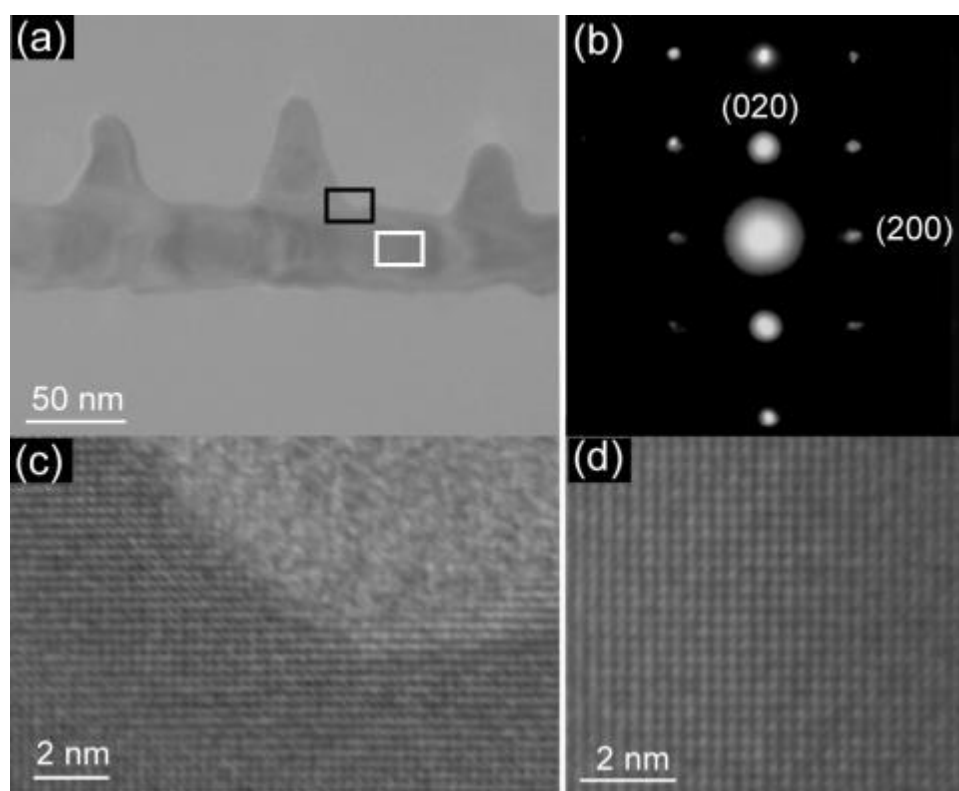


**Figure 6: Imaging of hyperbranched PbSe nanowires [22]**

(a) TEM image showing the nucleation of new branches from a main NW. (b) SAD pattern for the branching interface (black rectangle in a). (c) HRTEM at the branching interface shows the continuation of the same crystal lattice in the new NW branch. (d) HRTEM shows the rock salt structure of the main NW (white rectangle in a). [22]

Aside from these important findings, the group also discovered that they could control the diameter of the NW by changing the furnace temperature, or by performing the growth in a different location within the furnace with a different temperature. By growing at 350°C instead of 400°C, the diameter shrunk from roughly 100nm to about 60nm. By using a lower temperature to create smaller nanowires, it may be possible to achieve the domain size needed for solar cell applications.

A group led by Dr. Wang of the South China University of Technology has pursued development of a CdS nanorod based hybrid solar cell device [23]. They acknowledge that not much work has been done in this area by other groups due to the relatively high band gap of CdS (2.42 eV), which is in stark contrast to the low energy band gap of PbSe. However, the researchers decided to pursue CdS due to its high electron mobility.

The group looked to study the effect of several parameters on improving photovoltaic characteristics. One key finding was that the solvent used made a large impact on morphology (and subsequently on device performance). Depending on whether pyridine or chlorobenzene was used as the solvent for CdS and MEH-PPV, the morphology changed as shown in Figure 7. The effect of this change on device performance is summarized in Table 3.

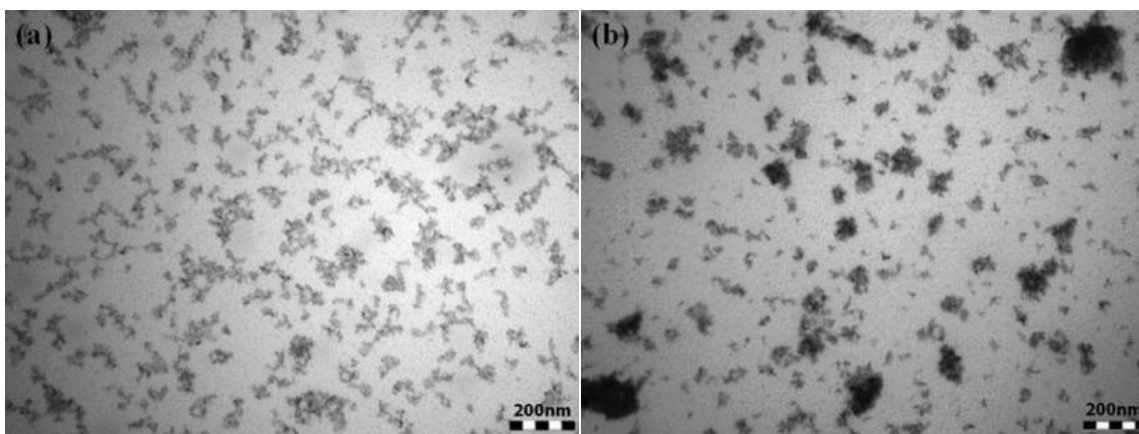


**Figure 7: Morphology of MEH-PPV:CdS films with different solvents [23]**

The morphology of the active layer changed greatly when the solvent was changed from (a) pyridine to (b) chlorobenzene. Particles in chlorobenzene were not evenly spread and tended to form agglomerates. [23]

**Table 3: Device properties for MEH-PPV:CdS solar cells with different solvents [23]**

solvent	$V_{oc}^b$ (V)	$I_{sc}^c$ (mA cm <sup>-2</sup> )	FF <sup>d</sup> (%)	ECE <sup>e</sup> (%)
pyridine	0.85	2.28	46.2	0.89
chlorobenzene	0.95	0.39	38.0	0.14

Wang's group also performed PL measurements on both types of films. Though both films showed significant PL quenching, the effect was greatest when the pyridine solvent was used. This greater PL quenching corresponds to more effective charge transfer at the interface. With this mounting evidence for pyridine being able to produce better device performance, the researchers performed FTIR and looked at the transmission spectra of the films before and after pyridine treatment. Peaks that corresponded to hexadecylamine (HDA) were found before the treatment, but the pyridine seemed to remove these peaks. The researchers concluded that pyridine is able to swap with the HDA molecules on the surface of the nanoparticles. This change in surfactant is responsible for the change in morphology, the better charge transfer, and indeed all the improved device characteristics. Therefore, attention must be taken to ensure that nanocrystals are covered by an appropriate surfactant when designing a hybrid solar cell.

Interestingly, the study done by this group showed that the morphology did not improve upon annealing. Furthermore, the dark current of the device remained unchanged, indicating that a 150°C treatment does not affect the molecular packing of the polymer. In spite of this, the photocurrent still showed a modest increase after heat treatment. Under simulated AM1.5 global solar conditions at an intensity of 100 mW/cm<sup>2</sup>, the  $I_{sc}$  increased from 1.25 mA/cm<sup>2</sup> to 1.46 mA/cm<sup>2</sup> after annealing at 150 °C for 20 min. Additionally, fill factor (FF) shows an increase from 37% to 45%, though  $V_{oc}$  remains unchanged at 0.85V. The group assumes that this annealing must somehow improve the interface between the nanorods and the polymer, leading to improved exciton dissociation.

A group from Imperial College, London, has fabricated devices using a blend of P3HT and TiO<sub>2</sub> nanorods [24]. The nanorods are capped with trioctylphosphine oxide (TOPO) and are processed from solution. The first important result this group found was that simply increasing the concentration of nanocrystals in their films, they could change the morphology. In general, they observed that a higher concentration of nanorods led to smaller domain sizes (even after annealing), which is favorable. Also, annealing the blend films is found to greatly improve the polymer–nanorod interaction at the interface. This improvement allows an increase in the charge separation yield, which is critical for these types of devices. The authors note that this type of improvement upon annealing is different from what is observed in the P3HT:PCBM system, where the main benefit comes from improved crystallization of the polymer phase and subsequent gains in hole mobility. For the nanorod-based devices annealing results in smoother films, higher  $J_{sc}$  and  $V_{oc}$ , which leads to improved photovoltaic device performance. Under simulated solar illumination, the device had photocurrent  $J_{sc} = 0.10 \text{ mA/cm}^2$ , open-circuit voltage  $V_{oc} = 0.70 \text{ V}$ , and a fill factor of 0.28, resulting in a power conversion efficiency of only 0.04%.

However, the group found a way to improve this further. In wondering why the devices produced such a low photocurrent, they questioned the impact of insulating trioctylphosphine oxide (TOPO) molecules on the surface of the nanoparticles. TOPO is used to improve the solubility of TiO<sub>2</sub> nanorods so they can be spin cast from solution. To perform a ligand exchange, the TOPO-capped nc-TiO<sub>2</sub> nanorods were co-dissolved with an excess of the ruthenium dye cis-bis(isothiocyanato) (2,20-bipyridyl-4,40-dicarboxylato)(2,20-bipyridyl-4,40-di-nonyl) ruthenium(II) or Z907. This amphiphilic dye could exchange TOPO due to the strong affinity of the carboxylic groups with the metal oxide surface. The alkyl chains of Z907 were able to help the dispersion of the rods in organic solvents such as chloroform, leading to a better device performance. While the photocurrent nearly doubled after this ligand exchange, the overall result is still poor. The authors think this suggests that transport within or between

nanoparticles limits performance. In particular, they propose that charge transport in the P3HT:TiO<sub>2</sub> nanorod blend films is limited by the presence of an intrinsic trap distribution mainly associated with the nanorods.

### 2.1.3.Unique Nanoparticles

As mentioned before, researchers want to attain a controlled morphology by altering the geometry of their nanoparticles. While nanorods/nanowires are a popular geometry, they are by no means the only possible answer. Some groups are experimenting with novel structures that could also lead to new breakthroughs. These researchers are looking to create more exotic shapes for their nanoparticles than the typical sphere. By creating a branched-type structure, they can attain more surface area for creating a junction as well as limit domain size to what can be crossed by exciton diffusion.

A group from the Chinese Academy of Sciences in Beijing has investigated the performance of a series of hybrid nanocrystal/polymer solar cells based on MEH-PPV and CdSe<sub>x</sub>Te<sub>1-x</sub> tetrapod nanocrystals [25]. Of the two materials, the CdTe has the lower band gap and also has higher absorption than CdSe. However, upon studying the effects of composition in devices made with nanocrystals having varying compositions, they found that in the end, CdSe would outperform any blend of the two. They obtained power conversion efficiency as high as 1.13% in MEH-PPV:CdSe tetrapods under illumination of AM 1.5, 80 mW cm<sup>-2</sup>. These results are shown in Table 4. For clarification, their nomenclature Na1 – Na3 refer to the varying compositions of CdSe<sub>x</sub>Te<sub>1-x</sub> used for the blends. Na1 has x=0.23, Na2 has x = 0.53, and Na3 has x=0.78.

**Table 4: Device parameters for varying compositions of CdSe<sub>x</sub>Te<sub>1-x</sub> [25]**

Nanocrystals in the hybrid solar cells	$V_{oc}$ (V)	$(J_{sc})$ (mA cm <sup>-2</sup> )	FF	$\eta$ (%)
CdTe	0.33	0.024	0.33	0.003
Na1	0.42	0.48	0.30	0.075
Na2	0.63	0.65	0.35	0.18
Na3	0.69	1.57	0.36	0.49
CdSe	0.69	2.86	0.46	1.13

Despite the fact that the composition did not show any dynamic or synergistic effects, several important results could be gleaned from this research. The first is shown in Table 5. Taking only CdSe:MEH-PPV, the researchers varied only nanocrystal loading. Often, a higher loading of nanocrystals can increase device efficiency by changing blend morphology. However, overloading the film is not desirable either, as it may become difficult for the phases to intermingle. Essentially, there is an ideal ratio that must be determined for each new material system.

**Table 5: Effect of NC loading on PCE for CdSe:MEH-PPV [25]**

CdSe:MEH-PPV (weight ratio)	1:2	1:1	4:1	7:1	9:1	16:1	20:1
PCE (%)	0.13	0.17	0.42	0.52	1.13	0.66	0.16

Additionally, the group took cyclic voltammetry measurements to determine band edge positions for the different compositions, and the result is shown in Figure 8. These findings shed some light on why CdSe performs best. Earlier it was mentioned that a type II heterojunction is required for charge separation. However, it may not be sufficient to have a small discontinuity between the two materials. The authors of this paper suggest that because the low position of the conduction and valence bands of CdSe contrasts better with the relatively high HOMO and



LUMO for MEH-PPV, more efficient charge separation can occur. This makes sense due to the larger difference in energy levels between the two materials.

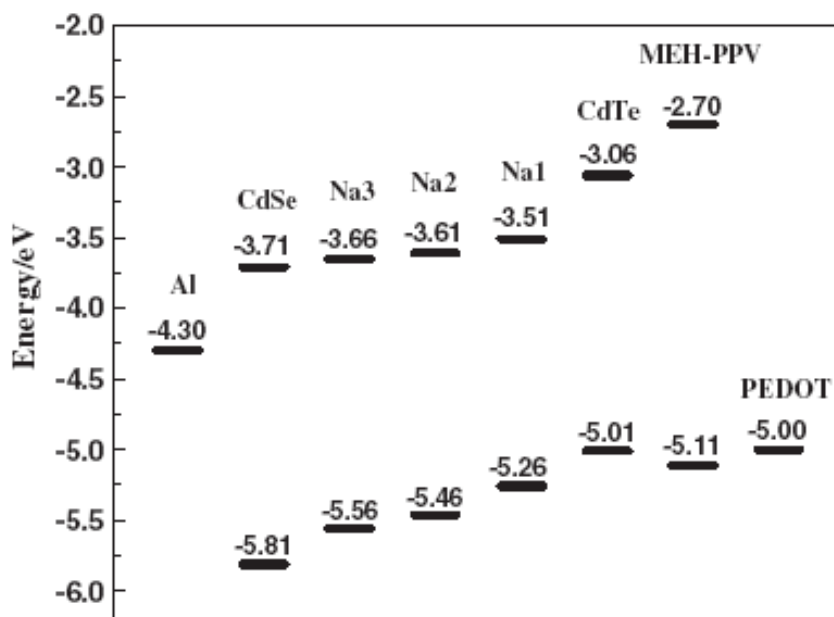


**Figure 8: Band edges for  $\text{CdSe}_x\text{Te}_{1-x}$  tetrapod nanocrystals, electrodes, and MEH-PPV [25]**

Conduction and valence band edges were determined using cyclic voltammetry measurements for all compositions of nanocrystals tested. For reference, the polymer and electrodes are also included. [25]

In conclusion, the group found that the photovoltaic properties show a regular change with composition: the open circuit voltage ( $V_{oc}$ ), short-circuit current ( $J_{sc}$ ), power conversion efficiency ( $\eta$ ) and IPCE of the devices all increase as Se content increases. By studying the absorption, charge separation and transport, they report that the change of the photovoltaic separation, which is caused by appropriate choice of the band level discontinuities between the polymer and the nanocrystal. This result is certainly an interesting one, and it would be even more beneficial to know if this effect could be extended even further. For example, if a test were done with a nanocrystal whose bands were even lower than CdSe, it would be interesting to note

if the benefit would still be seen or if there is some sort of attenuation to the benefit as the band offsets become large.

A group at University of California, Berkeley, has proposed another novel structure [26]. Their nanoparticles take on a shape similar to a sea urchin, shown in Figure 9. They call these structures hyperbranched nanocrystals, and their synthesis is a very simple solution process. These particles grow to be quite large, but the nature of their shape keeps domain sizes on the order of the exciton diffusion length. As a result, while maintaining the requirement on domain size, the particle automatically forms a straight network from cathode to anode, as the particle is so large that it stretches from one to the other on its own. Therefore, the morphology of the blend film is dictated by the shape of the nanoparticle itself, and these nanoparticles can form a monolayer if the correct ratio of NC to polymer is achieved. The buildup of a monolayer is shown visually in Figure 10a.

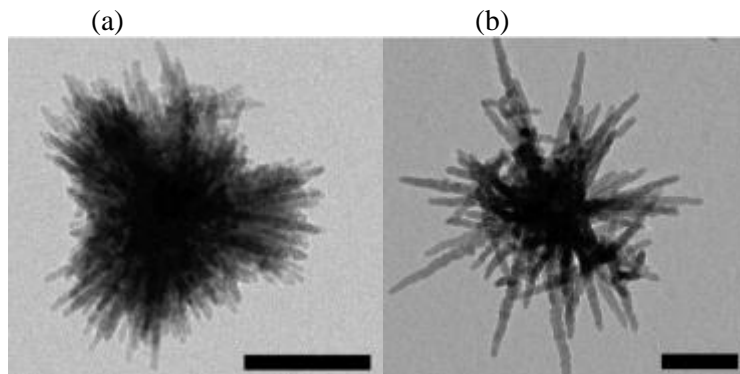


**Figure 9: Hyperbranched nanoparticles [26]**

TEM images show the structure of (a) CdSe and (b) CdTe hyperbranched nanocrystals. Scale bar is 100 nm. Due to the size, one particle is sufficient to stretch across the entire thickness of the film. [26]

For comparison's sake, the results of tests performed on these hyperbranched structures were compared with results of the same tests on solar cells using nanorod structures. The two different types of hybrid devices were tested at different nanoparticle loadings, from 0% up to

about 80% nanoparticles by volume. For every composition tested under an AM1.5 global radiation source, the open circuit voltage, short circuit current, fill factor, and power conversion efficiency were all higher in the hyperbranched nanoparticles than in the nanorods (Figure 10b).

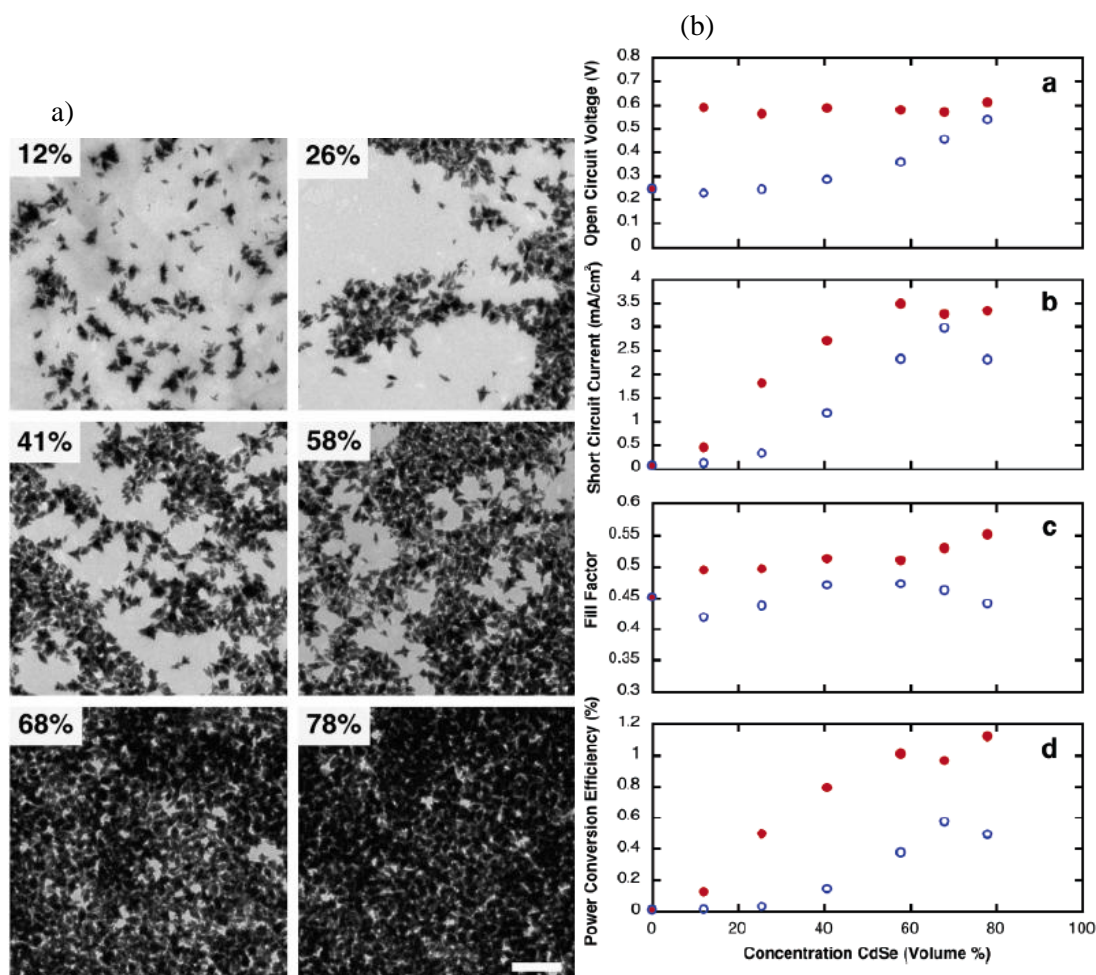


**Figure 10: CdSe hyperbranched nanocrystal morphology and performance [26]**

(a) TEM images show how the morphology depends on the nanocrystal loading. All percentages give the volume concentration of CdSe in the spin-casting solution. Scale bar is 500 nm (b) Hybrid solar cell characteristics for hyperbranched CdSe nanocrystal (solid circle) and nanorod (open circle) devices. [26]

The authors warn that there is one minor concern with this across the board outperformance – it is possible to increase the performance of the nanorods. However, their explanation of this detail brings out another advantage of the hyperbranched structures. The

nanorods can attain better performance if the morphology can be improved. However, this is difficult to achieve because that material system is highly sensitive to processing conditions. On the contrary, hyperbranched particles have decreased sensitivity to variation in loading concentration and processing. This is evidenced by the better fill factor, which relates to diode ideality and overall cell quality. The FF is also more consistent for the hyperbranched particles. These results show that the ease and consistency of processing along with morphology prescribed by the particle itself are great benefits to using these hyperbranched structures.

At the University of Minnesota, a group has demonstrated a quantum-dot sensitized nanowire solar cell [27]. Their system is based on photosensitization of ZnO nanowires much like a dye-sensitized solar cell, only they choose to use CdSe quantum dots. The photogenerated electrons are injected across the quantum dot-nanowire interface into the ZnO. In order to attach the CdSe to the ZnO, they use a short linker molecule, mercaptopropionic acid (MPA). This molecule is short in order to minimize the tunneling barrier for electron transfer. At the current time, this research is still beginning, so the holes are removed via a liquid electrolyte containing a redox couple in which the nanowires are bathed. In further research, this could potentially be replaced with a hole transport medium.

The group found that treating the ZnO nanowires with an oxygen plasma significantly enhanced the quantum dot adsorption. HRTEM images showed that more CdSe was able to attach to the surface of the nanowires after the treatment. To explain this, the researchers suggest that the plasma may be able to ionize the surface. Also, it may create dangling bonds through ion bombardment, or it might remove surface contaminants. Though the group is not totally sure of the exact reason, they did find evidence for decreased surface contamination through ATR-FTIR spectrum measurements. At any rate, the device performance increased by over an order of magnitude using the oxygen plasma treatment. Devices had  $J_{sc}$  of 1 to 2 mA/cm<sup>2</sup> and  $V_{oc}$  of 0.5 to 0.6 V when illuminated with 100 mW/cm<sup>2</sup> simulated AM1.5 solar spectrum. Internal quantum

efficiencies as high as 50-60% were achieved, and the overall power conversion efficiency was 0.4%. These numbers will likely improve with the further investigation of a proper hole transport medium.

Research done at Korea University shows that nanoparticles can also be attached to carbon nanotubes [28]. Specifically, this group took multiwalled carbon nanotubes (MWCNT) and used an acid bath to functionalize them. Afterward, the MWCNTs were washed and then immersed in a solution containing copper acetylacetonate and sulfur. By modifying the concentration of these precursors, the group was able to obtain different sizes of spherical nanoparticles, and eventually at higher concentrations they saw triangular nanoplates. Both of these are shown in Figure 11. Fabricating a simple sandwich structure device using poly(3-octylthiophene) (P3OT) as the organic hole conductor, the group ran photovoltaic tests. The short-circuit current density  $J_{SC} = 0.57 \text{ mA/cm}^2$ , open-circuit voltage  $V_{OC} = 0.32 \text{ V}$ , fill factor  $FF = 44\%$ , and power conversion efficiency = 0.08% under AM1.5 radiation. The group also noticed that photovoltaic devices fabricated from the blends of Cu<sub>2</sub>S-MWCNT and P3OT performed better than those fabricated using Cu<sub>2</sub>S NCs or MWCNTs alone. Improving electron transport from the photoexcited Cu<sub>2</sub>S NCs to the MWCNTs is the next step.

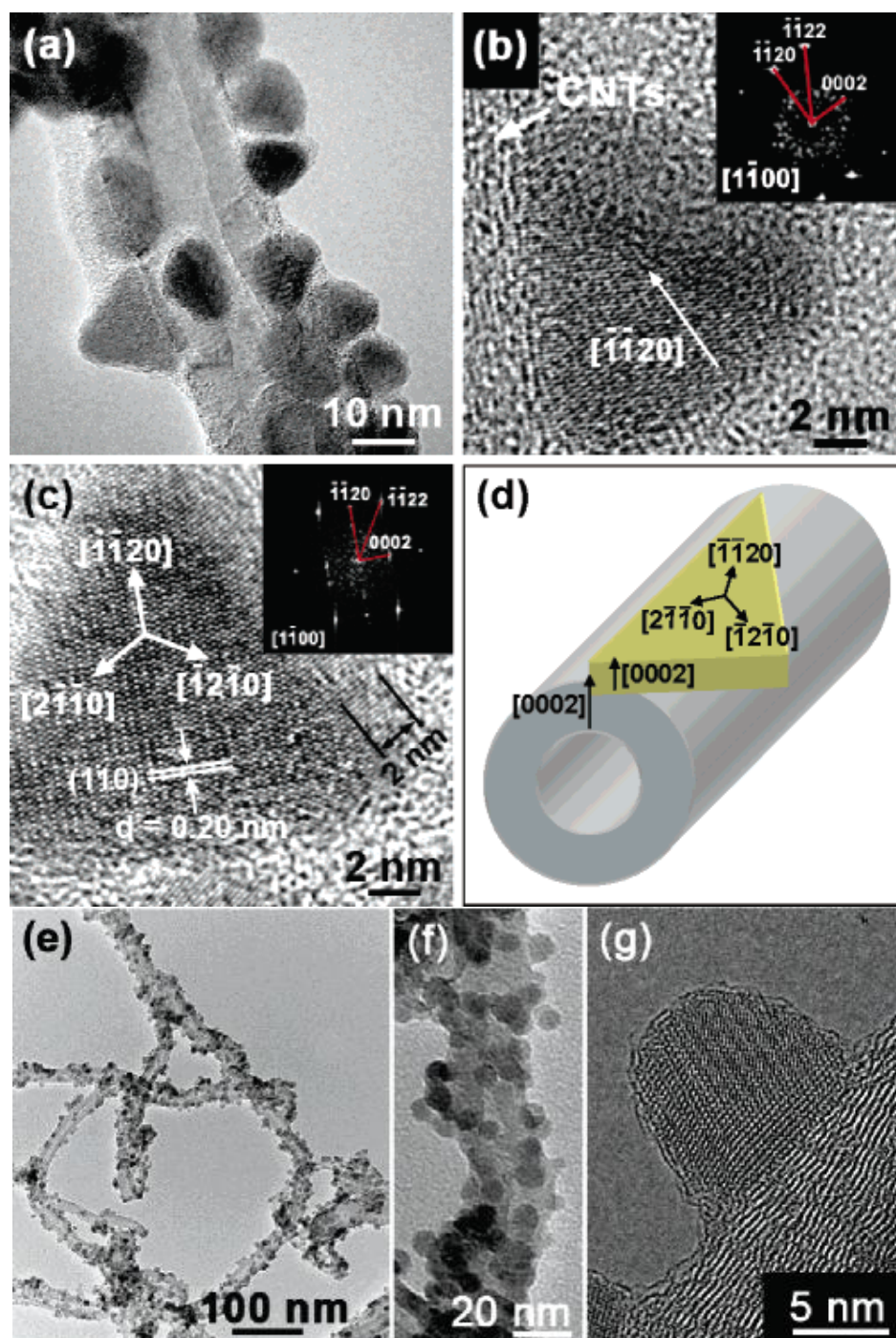


**Figure 11: CuS nanoparticles attached to MWCNTs [28]**

(a) Using TEM, one can see the triangular NCs attached to the MWCNT. (b) HRTEM shows how one face of the plate is bound to the nanotube. (c) One of the detached NCs shows a 2nm thick edge. [The insets show FFT ED patterns for determining crystallographic orientation.] (d) A schematic showing the orientation of the nanoplate attaching to the MWCNT. (e,f) TEM images showing the spherical NCs attaching to MWCNTs. (g) HRTEM shows a tight bond between the NC and the CNT. [28]

## **2.2. Time of Flight (TOF)**

Before describing the experiments performed, a summary of these measurement techniques is necessary. This allows a fuller understanding of the experiments undertaken in the remainder of this thesis. Here, the basic physics of the devices is studied in detail, and useful relationships are derived between mobility, lifetime, and measurable experimental parameters.

### **2.2.1. Current Mode TOF**

Since the Haynes-Shockley experiment of the early 1950's, scientists have had a reliable way to determine charge carrier mobility in their semiconductor samples. The technique is typically called a time-of-flight (TOF) measurement [3]. It involves taking a sample of a set thickness with electrodes on either side, applying a voltage across the sample, and injecting a pulse of carriers near one electrode. Either electrical or optical excitation can be used to inject carriers. Under the influence of the electric field, either electrons or holes will be swept across the entire distance of the sample, depending on the polarity of the applied voltage. If the transit time for this carrier packet can be determined, then the drift velocity (and thus the mobility) is easily obtained. We will call this technique "current mode" TOF since the mobility is determined from the current signal.

To determine the transit time, one must find a distinct feature in the voltage transient. For silicon and other ordered materials that were first studied with this technique, the voltage transient will have a plateau after the initial spike. After some time, the carriers are extracted and the signal returns to zero. The point where the plateau and extraction meet will look like a shoulder on the V-t curve. The transit time can be found from the time between this kink and the initial spike. Unfortunately, for disordered materials like the polymers we are interested in

studying, the transport is dispersive. The extraction and the initial spike blend together so that no plateau or kink can be discerned from a V-t plot. The solution is to plot on a log-log scale, after which a kink can be seen between two linear regions. Similar to the case of the ordered material, the transit time for a disordered material can be found from this log-log kink [29]. The difference in the appearance of these two kinks is shown in Figure 12.

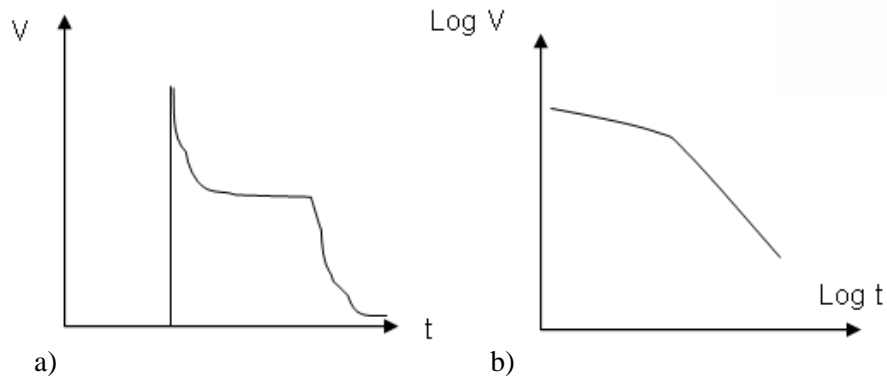


**Figure 12: TOF transients for non-dispersive and dispersive transport**

(a) In materials with non-dispersive transport, such as single crystal Si, a plateau with a defined shoulder makes finding transit time easy. (b) For dispersive transport, V-t curves must be plotted on a log-log scale to find a kink.

This technique has been applied to polymer based solar cells with some success. Dr. Yang's group at UCLA has studied the effect of composition and heat treatment on the performance of P3HT-PCBM solar cells [1]. Their sample thickness varies from 0.7 to 1.53  $\mu\text{m}$ . The applied bias varies from 0 to 20 V and they illuminate the transparent ITO electrode using a nitrogen laser with  $\lambda=337$  nm,  $\tau=4$  ns, and 10 Hz repetition rate. When varying their composition ratio, they found that the ideal ratio of P3HT:PCBM was 1:1, since it produced the highest measured mobility of  $\mu = 1 \times 10^{-4} \text{ cm}^2/\text{Vs}$ . Hole mobility was almost the same, but always lower than the electron mobility by a factor of about 20%, depending on the voltage used for the measurement.



Other groups have also performed similar current mode TOF studies on relatively thick samples of P3HT:PCBM. Dr. Ballantyne's group at Imperial College London has investigated the effect of P3HT molecular weight on device performance [3]. Their findings indicate that increasing the molecular weight of the polymer decreases the mobility, fill factor, and the power conversion efficiency of the cell. The mobility of both electrons and holes reduced at least an order of magnitude when molecular weight was increased from 13 kDa to 121 kDa, where Da is a dalton, or an atomic mass unit. The mobility for holes in these 1:1 ratio films ranged from  $\mu_h = 3 \times 10^{-5} \text{ cm}^2/\text{Vs}$  to  $4 \times 10^{-4} \text{ cm}^2/\text{Vs}$ , while the electrons ranged from  $\mu_e = 1 \times 10^{-5} \text{ cm}^2/\text{Vs}$  to  $1 \times 10^{-3} \text{ cm}^2/\text{Vs}$ .

In Korea, several groups have combined to study temperature dependent mobility behavior in P3HT:PCBM solar cells [2]. Their devices have a 1:1 ratio, a 1.1  $\mu\text{m}$  active layer thickness, and a 100 nm thick LiF:Al top contact. The devices were illuminated through the ITO electrode using a nitrogen pulse laser with  $\lambda=337 \text{ nm}$ . Voltages as high as 60 V were used to create the drift field. At room temperature, the mobility for holes ranged from  $\mu_h = 2 \times 10^{-5} \text{ cm}^2/\text{Vs}$  to  $5 \times 10^{-5} \text{ cm}^2/\text{Vs}$ , while the electrons ranged from  $\mu_e = 7 \times 10^{-5} \text{ cm}^2/\text{Vs}$  to  $2 \times 10^{-4} \text{ cm}^2/\text{Vs}$ . At temperatures up to 400K, it was found that mobility increases approximately one order of magnitude. This makes sense for this disordered material system with dispersive transport, as the primary carrier transport is believed to be a thermally activated short range "hopping" mechanism [30].

### **2.2.2. Integral Time-of-Flight (I-TOF) Theory**

The results from current mode TOF measurements are consistent with each other, giving some idea about the charge carrier mobility in these disordered materials. However, there is a limitation when attempting to use TOF to study thin film devices. Naturally, the measurement

circuit will have some response dependent on the RC time constant of the components. As the device thickness shrinks, the geometrical capacitance increases. Therein lies the problem – when the polymer film is no longer on the order of microns thick, the RC time constant of the measurement setup will be on the same order as the transit time one wants to observe.

In thick films, this is not so much a problem. A large thickness will mean a relatively small C but a relatively large  $t_{tr}$  so that  $t_{tr} \gg \tau_{RC}$  is upheld. However, for thin films,  $t_{tr}$  and  $\tau_{RC}$  may be on the same order [31]. This means that the kink seen on the graph in Figure 13 will not correspond directly to the transit time, but rather a convolution of the transit time and the RC decay time. This will invalidate the measurement, as proven by Juška [32].

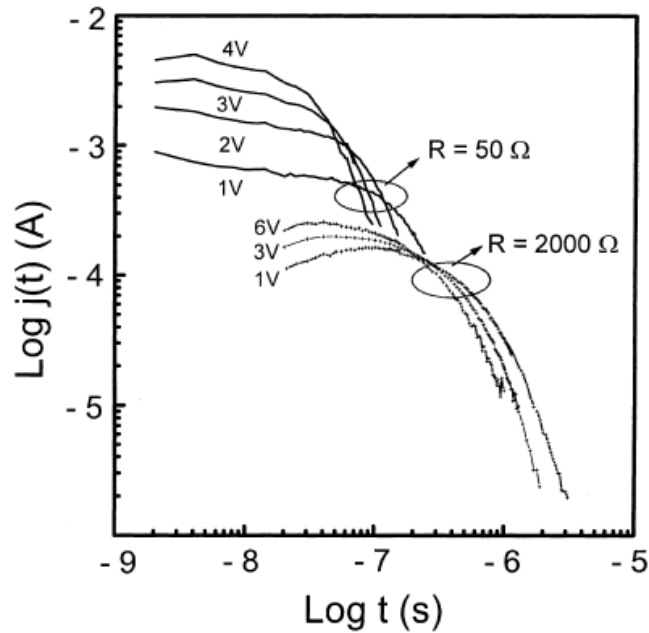


**Figure 13: Effect of RC decay on TOF measurements [32]**

The kink in a current mode TOF experiment may not directly measure the transit time if the RC decay occurs on the same timescale. Here, increasing the detection resistance (and thus  $\tau_{RC}$  of the measurement circuit) has changed the value of  $t_{tr}$  and invalidated the results. [32]

Therefore, an alternative technique is necessary for studying device-realistic thin films. Fortunately, such an alternative already exists. First developed for performing high sensitivity drift mobility measurements in amorphous semiconductors, the technique involves collecting

charge at the measurement electrode rather than measuring a current [33]. In 1988, Dr. William Spear wrote that he could extract the transit time of carriers by using the detection oscilloscope to determine the “integrated charge displacement.” Shortly after this paper, a group from eastern Europe led by Dr. Gytis Juška analyzed the physics of the technique, determining a method for extracting both the mobility and the mobility-lifetime product from the integrated transient [34]. Thus, the integral-mode time-of-flight (or I-TOF) measurement was born.

Juška based his derivations on work that had been done previously in the 1970's. Drs. Batra and Kanazawa of the IBM research laboratory had theoretically calculated the voltage transients in two similar situations – one concerned with trapping kinematics [35] and one concerned with the charge carrier dynamics after the photoexcitation of excess carriers [36]. The theoretical curves had features related to the material properties, and Juška linked this theoretical work to experimental measurement. The full derivations are given in the two papers cited above and will not be repeated here. However, a brief summary is necessary for context.

Both derivations are very similar. Starting with the study of photoexcitation, the assumed initial condition is that a photoconductor of thickness  $L$  is charged to an initial potential  $V_0$ . Charge has built up on the surface at  $x=0$  while the electrode at  $x=L$  is kept grounded. Under open circuit, there is no charge injected into the device, except when the illumination takes place. Furthermore, it is assumed that there are no free carriers inside the sample before the light pulse. When this light pulse strikes the sample surface at time  $t=0$ , it will generate free charge carriers at  $x=0$ . Some of these charge carriers will neutralize the surface charge, while the others are driven toward the grounded electrode by the electric field in the sample. These initial conditions are depicted in Figure 14.

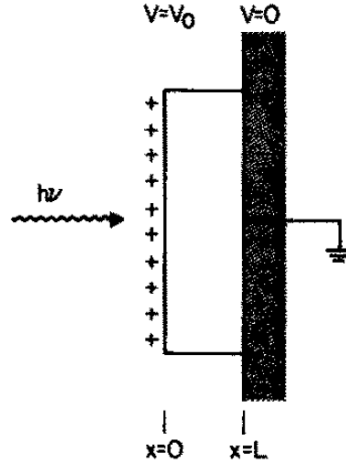


**Figure 14: I-TOF theoretical derivation schematic [36]**

The device is charged to an initial voltage  $V_0$ , causing charge to accumulate at the surface. When the light pulse hits, free charges are generated just inside the material, neutralizing the charge at the surface and traveling through the sample to the ground electrode at  $x=L$ . [36]

If trapping and diffusion are negligible, then the equations describing the transport of one type of carrier are the law of conduction,  $J_c(x,t) = q\mu n(x,t)E(x,t)$ , the continuity equation,  $\partial J_c(x,t)/\partial x = -q[\partial n(x,t)/\partial t]$ , Poisson's equation,  $\partial E(x,t)/\partial x = (4\pi q/k)n(x,t)$ , and the generalized equation for the total current,  $J = [\partial E(x,t)/\partial t] + (4\pi q\mu/k)n(x,t)E(x,t) = 0$ , which may be set equal to zero for this open circuit case.

To set up the boundary conditions, first define the charge inside the sample at any time,  $t$ , to be equal to  $Q$ . By definition, the integral  $Q(t) = q \int_0^L n(x,t) dx$  can determine the value of  $Q$  if the free carrier distribution is known. Now, define two points in time. Let  $t_{tr}$  indicate the transit time for the leading edge of carriers, and let  $t_F$  indicate when the final charge has reached the electrode at  $x=L$  and left the sample.

Finally, we can list our boundary conditions. Initially,  $Q(t) = Q_0$ ,  $0 \leq t \leq t_{tr}$ , where  $Q_0$  is the amount of charge injected by the light pulse. After the transit time, charge is extracted until

we reach a second boundary condition,  $Q(t) = 0$ ,  $t \geq t_F$ . We can also write that  $n(x,0) = 0$  because there are no free charges inside the sample before the light pulse. Also, recall that the initial voltage at the surface has been defined as  $V(t = 0) = V_0$ .

Using these boundary conditions and the four equations above, we can solve for the voltage transient,  $V(t)$ , in the region before the transit time of the leading carrier front. The result is  $V(t) = V_0 - \rho_0 \left(1 - \frac{1}{2} \rho_0\right) (V_0/L)^2 \mu t$ ,  $0 \leq t \leq t_{tr}$ . The term  $\rho_0 = Q_0/CV_0$  describes how much of the charge built up on the surface was injected by the light pulse. Taking the time derivative and substituting for the transit time  $t_{tr} = L^2/\mu V_0$ , we obtain  $\dot{V}(t) = -\rho_0(2 - \rho_0)(V_0/2t_{tr})$ ,  $0 \leq t \leq t_{tr}$ . For intense illumination, all of the charge on the surface should be injected. This situation corresponds to setting  $\rho_0 = 1$  and the equation for the initial slope of the voltage transient reduces to a simpler form:  $\dot{V}(t) = -V_0/2t_{tr}$ ,  $0 \leq t \leq t_{tr}$ . This is the crux of how to use ITOF to determine carrier mobility. From the initial slope of the voltage transient, calculate the transit time and use that to find the mobility [36].

On the other hand, a few modifications can be made to this derivation to account for the shape of the curve at longer times. After the carriers have been extracted, trapping is no longer negligible, as there will be a residual voltage present across the device. This voltage is due to the carriers which have been trapped on their way to the ground electrode. To characterize these traps, Kanazawa chooses the simple model of a single trap level with capture probability  $C_T$  and uniform concentration  $N_T$ . Therefore, the probability per unit time of a carrier falling into a trap should be given by  $C_T(N_T - n_T(x,t))$ , which would reduce to a constant if  $N_T \gg n_T$ . Assuming this holds true, the probability will be written as  $1/T$ , with  $T = 1/(C_T N_T)$ . If the traps are deep, then we can assume the charges are held indefinitely. This allows us to write

$\frac{\partial n_T(x,t)}{\partial t} = \frac{n(x,t)}{T}$  . Now that the traps have been described, we must remember to add a trapped charge density term to the Poisson equation.

Before solving the equations, the boundary conditions require slight modification to account for the traps. Initially, the electric field should be uniform everywhere in the material and equal to  $V_0/L$ . Also, the field should go to zero at the surface after all the charge has been injected. Finally, include the assumption that at time  $t=0$ , there are no free or trapped charges present anywhere in the material at  $x>0$ . With these slight modifications to include traps, we can now solve through the equations in the same manner as before.

Unfortunately, the answers are not as nice in this case, because combining all of the input equations yields a partial differential equation:  $\frac{\partial \varepsilon(x,t)}{\partial t} + \varepsilon(x,t) \frac{\partial \varepsilon(x,t)}{\partial x} = -\frac{\varepsilon(x,t)}{\tau} \ln \varepsilon(x,t)$ .

This PDE is a form of Lagrange's linear equation, and its exact solution is an arbitrary function of two arguments. However, greater usefulness and simplicity can be attained by solving the equation in certain limiting cases.

Looking at the final state, nothing varies with time. This allows us to drop the first term in the equation above when solving for the final state,  $\varepsilon(x,\infty)$ . After integration, we obtain  $E_1[-\ln \varepsilon(x,\infty)] = x/\tau$ , where  $E_1[A] \equiv \int_A^\infty (e^{-z}/z) dz$ ,  $A > 0$ . This is called the exponential integral, and it can be computed numerically with software such as Mathematica® or looked up in a table of values.

Now, the residual voltage is found in a similar fashion. By integrating the differential equation (after dropping the time derivative term) with respect to  $x$  from 0 to 1, the result is  $E_1[-2\ln \varepsilon(1,\infty)] = v_R/\tau$ , with  $v_R$  the residual voltage. It should be noted that all the variables

in this derivation have been normalized to unitless quantities – so  $v_R$  and  $\tau$  are unitless counterparts to  $V_R$  and  $T$ .

If we take  $E_1[-\ln \varepsilon(x, \infty)] = x/\tau$  and let  $x=1$ , then we can plug the result into  $E_1[-2\ln \varepsilon(1, \infty)] = v_R/\tau$  and determine the relationship between  $v_R$  and  $\tau$ . This yields a universal curve between  $v_R$  and  $\tau$ . Thus, if  $v_R$  is measured, then  $\mu T$  can be determined by reading this universal curve and plugging into  $\mu T = L^2 \tau / V_0$ . This is how to determine the mobility-lifetime product from the residual voltage of an I-TOF measurement [35].

### 2.2.3. Integral Mode TOF Experiments

Many groups have used I-TOF to study the mobility of the charge carriers in their devices, particularly those groups working with thin films. Typically, these groups will either use a charge collection mode oscilloscope, or they will simply connect their device in parallel with a capacitor to collect the charge. The oscilloscope reads the charge on the other side of the capacitor. To provide the initial electric field, either a DC voltage source or a pulsed voltage source is connected to the device and capacitor in series through a resistor. Devices are illuminated through the transparent electrode. A schematic is given in Figure 15.

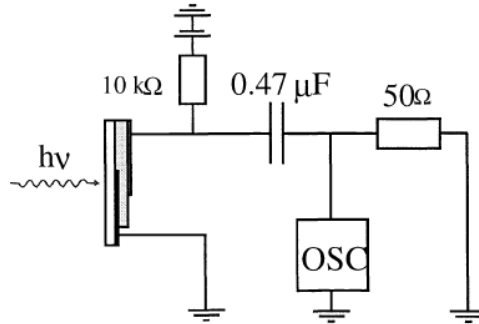


**Figure 15: Circuit Schematic for Integral mode Time-of-Flight [37]**

The integral TOF circuit consists of just resistors and capacitors, with output over an oscilloscope. [37]

In a review of charge transport in polymer/fullerene solar cells, Pivrikas notes that I-TOF performed on a P3HT:PCBM solar cell device yielded a mobility value of  $\mu_n = 4 \times 10^{-3} \text{ cm}^2/\text{Vs}$  [4]. In a separate test, Pivrikas also attained a value of  $\mu_n = 3 \times 10^{-3} \text{ cm}^2/\text{Vs}$  [38]. There are also several instances in the literature where groups have tested P3HT with no PCBM added. Since P3HT is a hole conductor, it typically has a high hole mobility (for a polymer). This is verified by Juška, who used I-TOF to measure a hole mobility of  $\mu_h = 1 \times 10^{-2} \text{ cm}^2/\text{Vs}$  in regio-regular P3HT [39]. Österbacka conducted similar measurements and has obtained  $\mu_h = 8 \times 10^{-3} \text{ cm}^2/\text{Vs}$  [37].

### 2.3. Charge Extraction by Linearly Increasing Voltage (CELIV)

Unfortunately, since its development in the early 1990's, the I-TOF technique has run into several problems. The problems mainly occur in samples with a relatively high dark conductivity, such as P3HT:PCBM. One of these problems is that the material's dielectric relaxation time ( $\tau_\sigma$ ) should be longer than the delay between the voltage and light pulse. Relatively high bulk conductivity indicates that this is probably violated. Indeed, capacitance measurements typically yield higher values than the geometrical one, even in the MHz range, proving that the electric field is redistributed and concentrated in the contact regions. This means that I-TOF mobility values may often be over-estimated [7]. Additionally,  $\tau_\sigma$  must be longer than the transit time for an accurate measurement. If not, then the equilibrium carriers may redistribute the electric field faster than  $t_{tr}$  and invalidate the assumption of a homogeneous electric field. There is a great deal of complexity in this seemingly simple measurement.

Luckily, Juška's group found a way around this problem. Rather than use a light pulse and a square voltage pulse, he simply decided to extract the equilibrium carriers using a triangular voltage ramp. They named the new technique CELIV after how it works: charge extraction by a linearly increasing voltage [7]. Again, the full derivation of this technique can be found in the



paper just referenced. I will only summarize the important points to allow the reader to appreciate better the experimental results later in this paper.

### 2.3.1. CELIV theory

The theoretical model assumes a sample of thickness  $d$  with a blocking electrode at  $x=0$ . The equilibrium free carrier density is  $n$ . As a triangular voltage ramp is applied, the equilibrium carriers will move toward the opposite electrode and get extracted. This will create a depletion region from  $x=0$  to  $x=L(t)$ , and this depletion region will grow as time increases and more carriers are extracted.

The equations used are essentially the same as in the I-TOF derivations. The Poisson equation and continuity equation are integrated over  $x$  from 0 to  $d$ . Combining these two results with  $V(t) = At = \int_0^d E(x,t) dx$ , where  $A$  is the slope of the voltage ramp, the Riccati equation for

$l(t)$  is found to be  $\frac{dl(t)}{dt} + \frac{\sigma}{2\epsilon_0 d} l^2(t) = \frac{\mu A t}{d}$ . Next, the generalized current equation

$j(t) = \epsilon_0 \frac{dE(x,t)}{dt} + \sigma(x,t)E(x,t)$  is averaged over  $x$ . Solving those two equations

simultaneously yields a solution for the shape of the transient current. This theoretical shape is illustrated in Figure 16 [39].

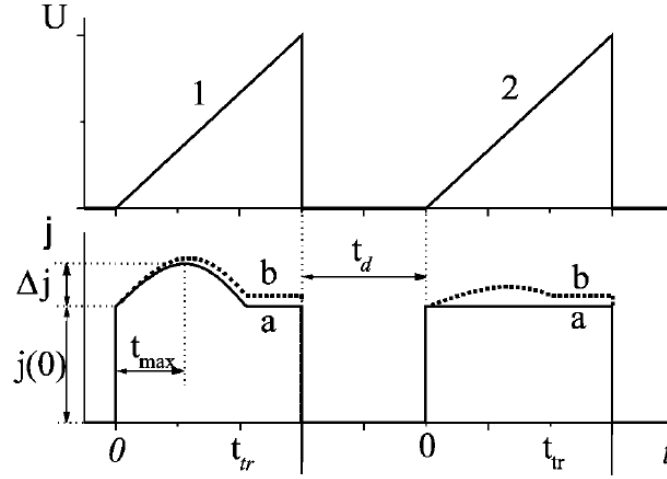


**Figure 16: Theoretical applied and output voltage signals for CELIV [39]**

At top, a triangular voltage ramp is applied to the sample. Due to sample capacitance, a displacement current with magnitude  $j(0)$  is seen immediately. The extraction of equilibrium carriers is shown by a current peak above the constant displacement current. Transit time is calculated from the peak time. A second ramp after the first can investigate how quickly equilibrium is recovered. [39]

Again, the most useful solutions are in certain limiting cases, where we can obtain an analytical form. For low conductivity material, when  $\tau_\sigma = \epsilon\epsilon_0/\sigma \gg t_{tr}$ , the extracted charge does not change the electric field distribution much, and we obtain a simplified piecewise equation for  $j(t)$ . The maximum of this transient occurs at a time which can be calculated and related to the transit time. A similar limiting case occurs when  $\tau_\sigma \ll t_{tr}$  for high conductivity samples. For samples of moderate conductivity, numerical analysis must be done. Luckily, Juška has already performed this numerical calculation and come up with a correction factor. The resulting equations for the transit time have been solved for mobility below [4]:

$$\left\{ \begin{array}{ll} \mu = K \frac{d^2}{At_{\max}^2}, & \Delta j \ll j(0) \\ \mu = K \frac{d^2}{At_{\max}^2 (1 + 0.36 \Delta j / j(0))}, & \Delta j \approx j(0) \\ \mu = \frac{d^2 j(0)}{At_{\max}^2 \Delta j}, & \Delta j \gg j(0) \end{array} \right.$$

Note that the three regions for conductivity can be discerned by the relative magnitudes of the displacement current  $j(0)$  and the extraction current  $\Delta j$  in Figure 16. In these equations,  $K$  is a constant which is 2 for surface generation of photocarriers and  $2/3$  for volume generation. Hence, the CELIV measurement is as simple as connecting a linearly increasing voltage to the sample, measuring the output current through a resistor, and determining the mobility from the time of the maximum extraction current by using one of the above equations [7].

Moreover, in the case that there are not enough equilibrium carriers, or one wants to study the behavior of photogenerated free carriers, this technique can be combined with a laser pulse just before the start of the voltage ramp. In this case, it is called photo-CELIV. These two techniques offer a simple and accurate way to probe the charge transport properties of a wide range of materials.

There is one more issue. In general, CELIV can only measure the majority carriers [7]. In the case of a material that is either p or n-type, it is simple to discern which mobility is being measured by this technique. However, photo-CELIV generates both types of carriers. In a material such as P3HT:PCBM, we must try to distinguish between the electrons and hole contributions. If the two carriers have greatly different mobilities (say they are different by a factor of 5), then two peaks may be visible on the CELIV plot. If not, then the two peaks will overlap. This is generally what happens for P3HT:PCBM solar cells, as they have been designed to have closely matched electron and hole mobilities for peak performance. In this case, the convoluted peak is generally attributed to the faster carriers, which tend to be the electrons. This has been reported many times in the literature [4, 5, 7]. One group even pointed out that the detection of only one peak indicates a balanced mobility, and that therefore the resulting mobility is descriptive of both electrons and holes [40].

### 2.3.2. CELIV Experiments

Many groups have taken up CELIV studies. It seems to be gradually replacing TOF style measurements. This could be in part due to the simplicity of the experimental setup. The only equipment necessary is a triangle pulse generator. A standard oscilloscope can measure the output voltage. If desired, a resistor can be added to the circuit to change the output impedance for signal detection. This experimental layout is given in Figure 17 [39].

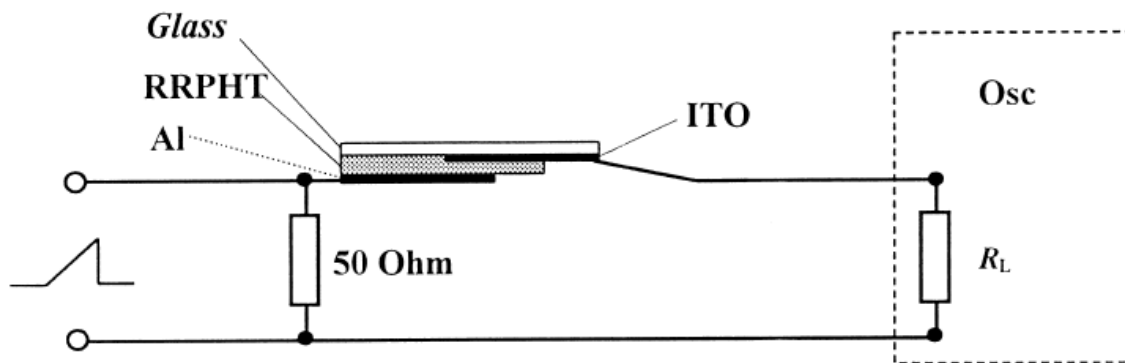


Figure 17: Circuit schematic for CELIV experiments [39]

The CELIV experiment is even simpler than the integral TOF setup. No capacitance is necessary, and the output signal may be dropped over a load resistance or fed directly to the oscilloscope in its high impedance setting. [39]

In his charge transport review of polymer/fullerene solar cells, Pivrikas also performed CELIV measurements. His results for P3HT:PCBM yielded  $\mu_n = 2 \times 10^{-4} \text{ cm}^2/\text{Vs}$ , which is a order lower than the I-TOF results [4]. Similar results were obtained a year earlier by Sliaužys, who measured  $\mu_n = 3 \times 10^{-4} \text{ cm}^2/\text{Vs}$  [5]. As with the I-TOF measurements before, P3HT has been measured by itself with no PCBM using the CELIV technique. Kažukauskas found a hole mobility of  $\mu_h = 1 \times 10^{-4} \text{ cm}^2/\text{Vs}$  [6], while Mozer's values were between  $10^{-3}$  to  $10^{-4} \text{ cm}^2/\text{Vs}$  [41].

## Chapter 3

### Experimental Details

All TOF measurements were carried out in the Laser Center in room 103 Research West. CELIV measurements were taken both at the Laser Center and in the Chemistry building, in collaboration with Dr. John Asbury's group.

#### 3.1. P3HT:PCBM Device Structure

Devices were fabricated using a bottom-up approach with the facilities in room 104, EES Building. All solar cells were made with a simple sandwich structure. The device schematic is shown in Figure 18.

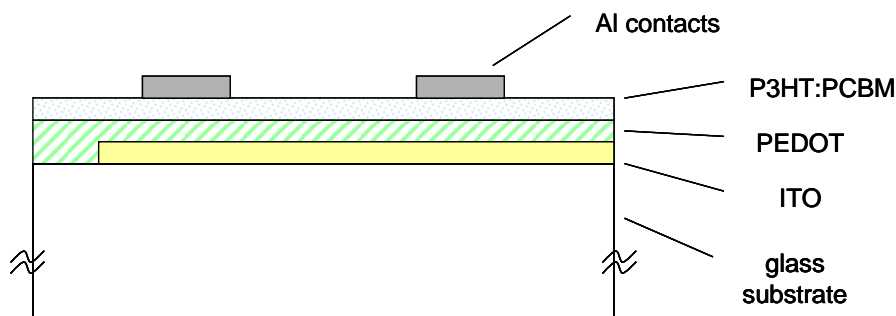


**Figure 18: Schematic of P3HT:PCBM test device**

A thin coating of ITO is applied to the glass for a bottom electrical contact. To improve hole transport, an additional layer of PEDOT:PSS is added on top of the ITO to complete the bottom electrode. The active layer is spin coated from solution and the top aluminum electrodes are thermally evaporated through a shadow mask. Layer thicknesses are 150 to 200 nm for ITO,

80 nm for PEDOT, and  $\sim 180$  nm for Al. The thickness of the active layer can be controlled by the amount of time the solution is spin coated, but is usually between 150 to 200 nm.

A clear glass substrate is used because this sample is designed to be illuminated from the back side. This improves the contact between the bottom electrode and the active layer, since the work function of PEDOT:PSS corresponds to the valence band of P3HT at 4.9 eV [42], allowing for an ohmic contact with good hole injection. Aluminum contacts are used at the top because the work function for aluminum matches the conduction band for PCBM [43]. The Al contacts are circular with a 3 mm diameter. A band diagram of the device is given in Figure 19.

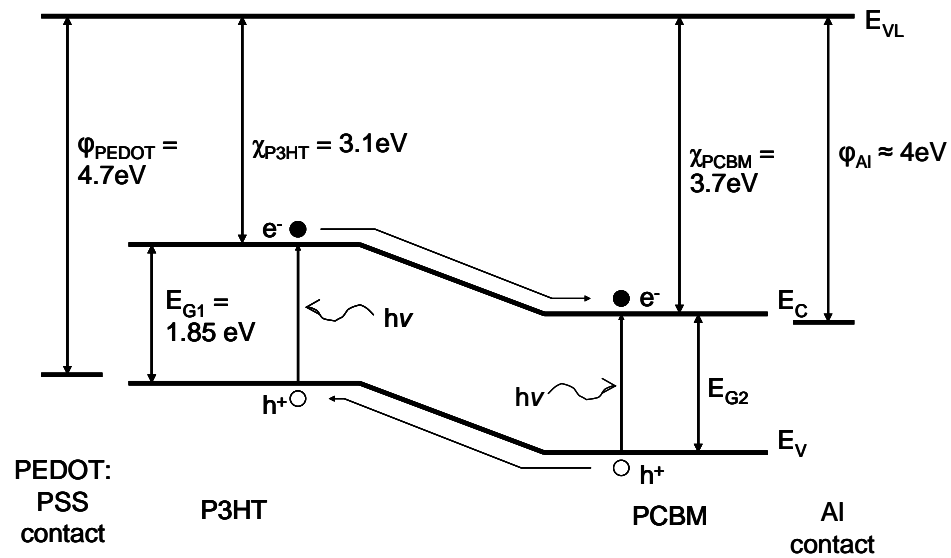


**Figure 19: Band diagram for P3HT:PCBM**

The absorption of a photon excites an electron-hole pair across the bandgap. The junction accelerates charges toward the contacts. In this material system, the process is slightly more complicated because the nanocomposite is a bulk heterojunction, so these junctions exist all throughout the device.

### 3.2. I-TOF Experimental Setup

Integral-mode TOF measurements follow the basic design outlined in Figure 15. A laser pulse is incident on the ITO side of a test sample. Two different lasers were used for this work. At high intensity, a femtosecond laser passed through an Optical Parametric Amplifier yields a laser output at 530 nm with a 1kHz repetition rate and a power of up to 600mW. For low intensity studies, an Nd:YAG diode laser with a 10kHz repetition rate and 100mW output at 1064 nm was frequency doubled using a potassium dihydrogen phosphate (KDP) crystal. The yield of green light at 532 nm was approximately 2.5 mW. Infrared and green light are separated through a series of dichroic lenses, so that the samples are illuminated only by the green light.

The ITO electrode is contacted simply by using an alligator clip to punch through the active layer. On the other side, the aluminum must be contacted with a soft copper wire. Thin copper wire is coiled around a probe with x-y-z movement. Once adequate springiness is obtained, a loop is formed at the end of the spring. The loop contacts the Al electrode without destroying it, while the spring compression keeps the contact stable enough to conduct measurements.

Following the guide of Figure 15, a power supply was put in contact with the aluminum electrode through a 10k $\Omega$  resistor. For initial measurements, this power supply was a DC voltage source. However, I-TOF studies are best performed with a pulsed voltage source and minimal elapsed time between the application of the voltage and the laser pulse [32]. To accomplish this, a digital delay generator was acquired. The infrared laser light that had been separated from the green was absorbed by a silicon photodiode. This signal triggered the delay generator, which output a transistor-transistor logic (TTL) pulse. The TTL pulse, in turn, triggered an Agilent 33220A function generator to output a square 5V pulse of 20  $\mu$ s duration. This was the signal

applied to the Al electrode. Biasing the diode in reverse like this ensures that electrons are the collected signal, so it is the electron mobility that is measured.

The Al electrode also connected to the capacitor depicted in Figure 15. For most measurements, a value of 0.47  $\mu\text{F}$  was used. Selecting this value by testing many different capacitances was one of the first experiments performed. This will be discussed further in later chapters. The back side of the capacitor was connected to the oscilloscope through a 50 $\Omega$  terminator. Voltage transients were stored on the oscilloscope and analyzed by the principles in the literature review, with the aid of Excel®, Origin®, and Mathematica® software.

### 3.3. CELIV Experimental Setup

The basic design for the CELIV measurements has also been described in the literature review. A circuit schematic can be found in Figure 17. For photo-CELIV measurements, the low intensity Nd:YAG diode laser described in section 3.2 was used. The green light was used for excitation while the infrared light again triggered the delay generator and function generator. This time, the function generator output a voltage ramp. The baseline of the ramp had a -1V offset in order to account for the open circuit voltage of the photocell. After a duration of 20  $\mu\text{s}$ , the maximum voltage reached was 8V.

The positive voltage ramp was connected to the Al electrode through the soft copper wire contact. The ITO electrode took the signal to the oscilloscope. Any load resistance could be used, but in this case the load resistance of the oscilloscope itself was sufficient to detect a signal. During the photo-CELIV measurements, the light pulse was incident on the ITO electrode. For all practical purposes, the light pulse and start of the voltage ramp were instantaneous. As in the case of I-TOF measurements, the data stored on the oscilloscope was analyzed based on theoretical equations previously mentioned in the literature review.



In addition to CELIV measurements performed with our own quick setup, we collaborated with a group in the Chemistry department here at Penn State who have been making CELIV measurements for about a year. There are a few significant differences in their experimental setup. First, their laser is an Nd:YAG laser at a much higher intensity, but it has been attenuated to 0.1mJ per pulse. Pulse duration is 4 to 6 ns with a 20 Hz repetition rate. The samples are contacted in the same manner as our own experiments – copper wire soft contact for the Al electrode and alligator clip for the ITO electrode.

Now, the entire sample is enclosed in a Bell jar and a vacuum hose is attached to evacuate the sample chamber. The Bell jar is transparent to the visible laser radiation, so the sample can still be illuminated at the ITO side in the usual way. This vacuum jar technique was developed to combat photobleaching and increase the lifetime of each sample. Photobleaching is the effect that when intense laser light hits the polymer, any oxygen in the vicinity will start to degrade the sample. Therefore, this vacuum chamber is likely to be a significant improvement to the experimental setup.

Finally, the signal leaves the sample and reaches a varistor, set to approximately 1 M $\Omega$ . The oscilloscope reads the voltage drop over the varistor as the CELIV signal. Both CELIV and photo-CELIV measurements were taken.

## Chapter 4

### Integral TOF Results

The first problem we tackled was simply to measure a signal similar to the ones found in the literature. The main features of the voltage signal in I-TOF are an initial linear slope and an eventual plateau, or residual voltage. The main hindrance in detecting the signal at first was that the dielectric relaxation time of our material is fairly short. This means it did not hold the plateau voltage for very long, and so the timescale on which we had to zoom in to see the features was in the nanosecond regime. However, when we did zoom in correctly, we were able to see a voltage trace very similar to the literature, both in theory and experiment. The following two figures compare our voltage signal to the literature.

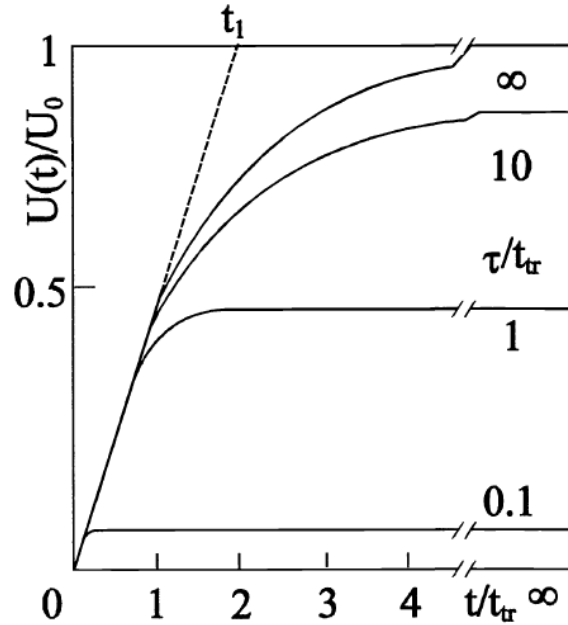
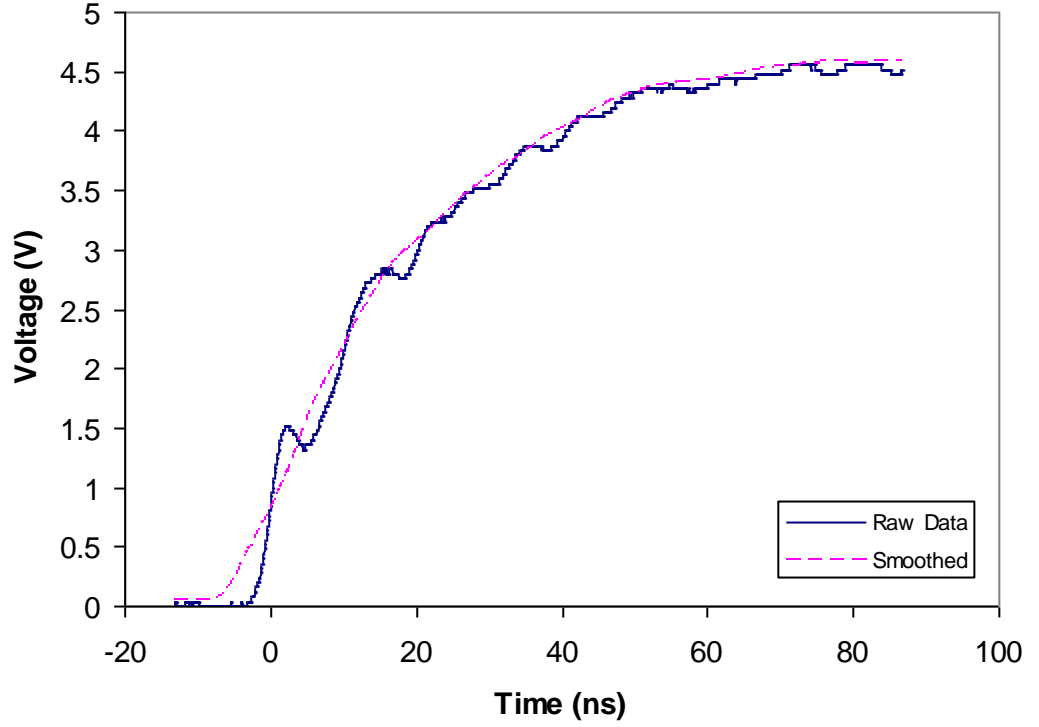


Figure 20: Integral TOF – literature voltage transients [37]

Theoretical voltage transients for I-TOF show the initial slope and plateau voltage. For negligible trapping, the plateau voltage would equal the applied voltage. As suggested by the different curves for different values of  $\tau$ , the carrier lifetime can be determined from the value of the residual voltage [37].



**Figure 21: Integral TOF – experimental voltage transient**

The solid line with the ripples is the raw data signal. The source of the ripples may be electrical noise in one stage of the experimental setup, or it might originate from some parasitic resistances and capacitances.

Almost immediately, we noticed that the signal had some ripples in it. We were worried that this would complicate the measurement of the initial slope. However, we took the data and smoothed it using adjacent averaging of data points. The results are visible above in the dotted line in Figure 21. Once the initial slope is known, the equations  $\dot{V}(t) = -V_0/2t_{tr}$ ,  $0 \leq t \leq t_{tr}$  and  $t_{tr} = L^2/\mu V_0$  from the literature review section can be combined to determine the carrier mobility. In a series of seven separate measurements on the same sample, we calculated a mobility of  $\mu_n = (5.61 \pm 0.044) \times 10^{-4} \text{ cm}^2/\text{Vs}$  using smoothed data, and a value of  $\mu_n = (5.52 \pm 0.05) \times 10^{-4} \text{ cm}^2/\text{Vs}$  using a best fit line to the original data. Due to overlapping confidence

intervals, these values show no statistical difference. Therefore, we were able to use smoothed data throughout our integral TOF experiments to allow for easier analysis.

The next task was to find a suitable capacitance value for the capacitor used to collect the charge (see circuit schematic in Figure 15). To test this, we tried measuring the mobility over a wide range of capacitance values. As it turns out, all the capacitors we tried yielded essentially the same value for mobility. These results are shown in Table 6. For all future experiments, we settled on using 0.47  $\mu\text{F}$  in order to match another group in the literature [37].

**Table 6: Integral TOF – dependence of mobility on collection capacitance**

C ( $\mu\text{F}$ )	$\mu(\text{cm}^2/\text{Vs})$
0.1	$5.67 \times 10^{-4}$
0.2	$5.63 \times 10^{-4}$
0.47	$5.55 \times 10^{-4}$
1	$5.64 \times 10^{-4}$
4.7	$5.58 \times 10^{-4}$
10	$5.57 \times 10^{-4}$
470	$5.58 \times 10^{-4}$

Following this, we were able to begin studying the carrier mobility in our devices. In addition to simply calculating the mobility for any of our devices which needed it, we tried to study the effect of certain parameters on the measured values. The two parameters varied were voltage and light intensity.

Voltage transients were collected from many samples, varying the applied voltage from  $V_0 = 1$  to 15 V. As expected, the slope and plateau voltage changed as voltage was increased. Illustrative results from one sample are given in Figure 22.

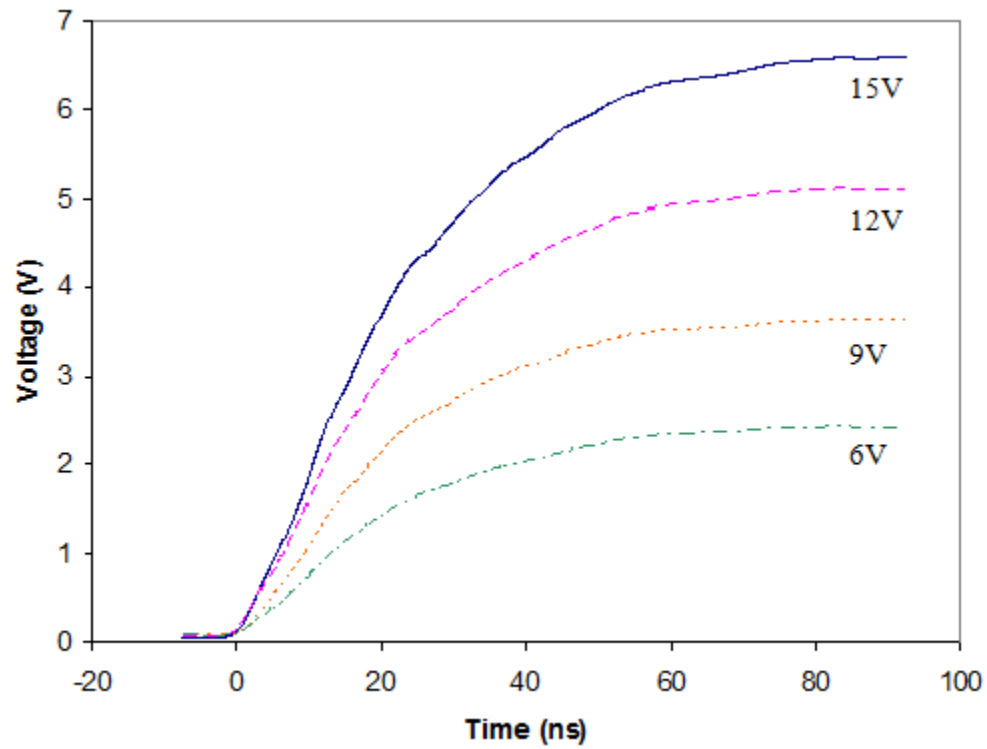


**Figure 22: Integral TOF – voltage transients for several different applied voltages**

As expected, an increased supply voltage will increase the charge stored at the surface of the sample, thus increasing the height of the voltage plateau. Notice also that the slope of the curves change.

When we conducted our mobility-voltage studies, each sample showed a negative dependence of mobility on applied voltage at room temperature. Unfortunately, we did not have the capability to get down in cryogenic temperatures as other groups did in literature to show a positive correlation [6, 40]. The results for two different samples are shown in Figure 23.

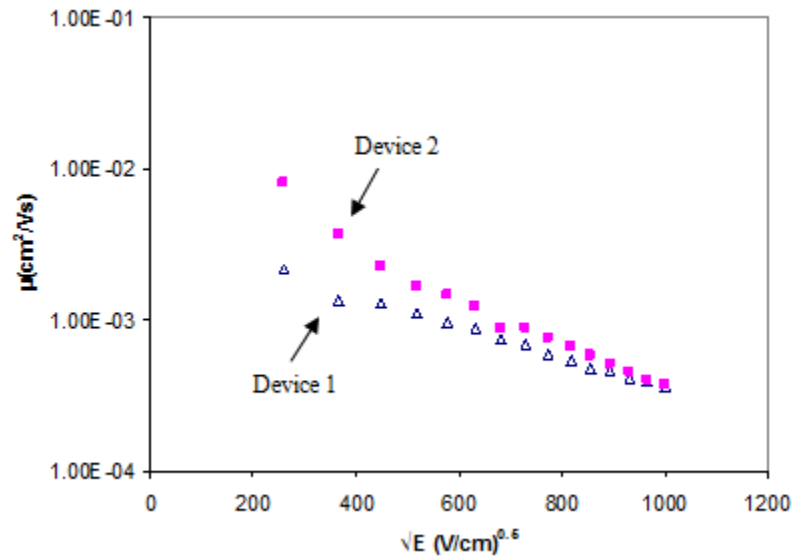


**Figure 23: Integral TOF – mobility dependence on electric field**

The mobility decreases as electric field increases for two different devices. The plot correlates  $\log \mu$  with  $\sqrt{E}$  to find a linear relationship. This Poole-Frenkel plot will be discussed further in Chapter 6.

Dependence of mobility on light intensity was also studied. No appreciable difference was found using various intensities from the femtosecond laser. Mobility measured using the much weaker diode laser was reduced by a factor of 4, as shown in Figure 24.

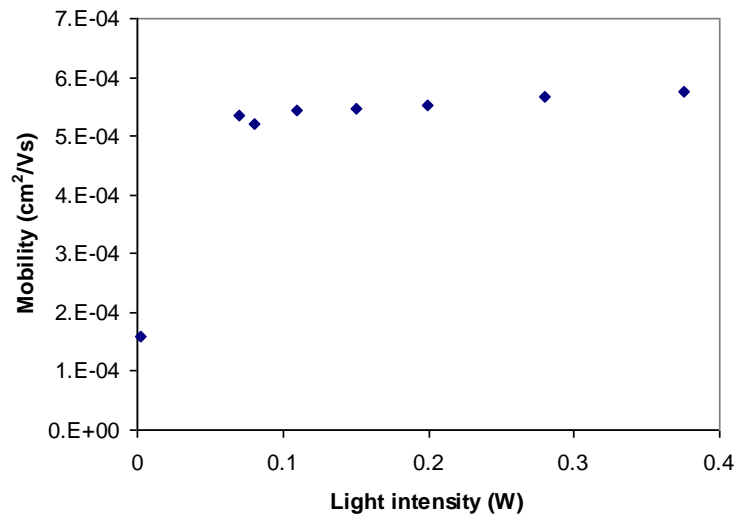


**Figure 24: Integral TOF – mobility dependence on light intensity**

Little variation is seen with decreasing light intensity until the much weaker diode laser is used.

## Chapter 5

### CELIV Results

Results of initial CELIV tests in the laser center look promising. From the very first measurement taken, the curves collected have looked very similar to what is found in the literature. This is shown below in Figure 25. Further discussion on the shape of the curve is saved for Chapter 6.

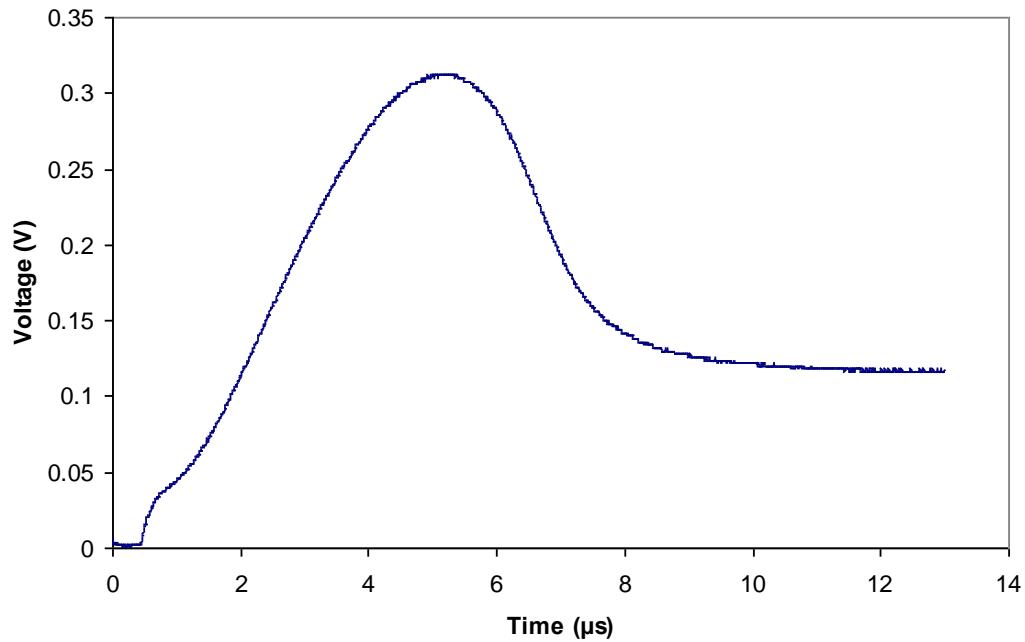


**Figure 25: Photo-CELIV – sample voltage signal**

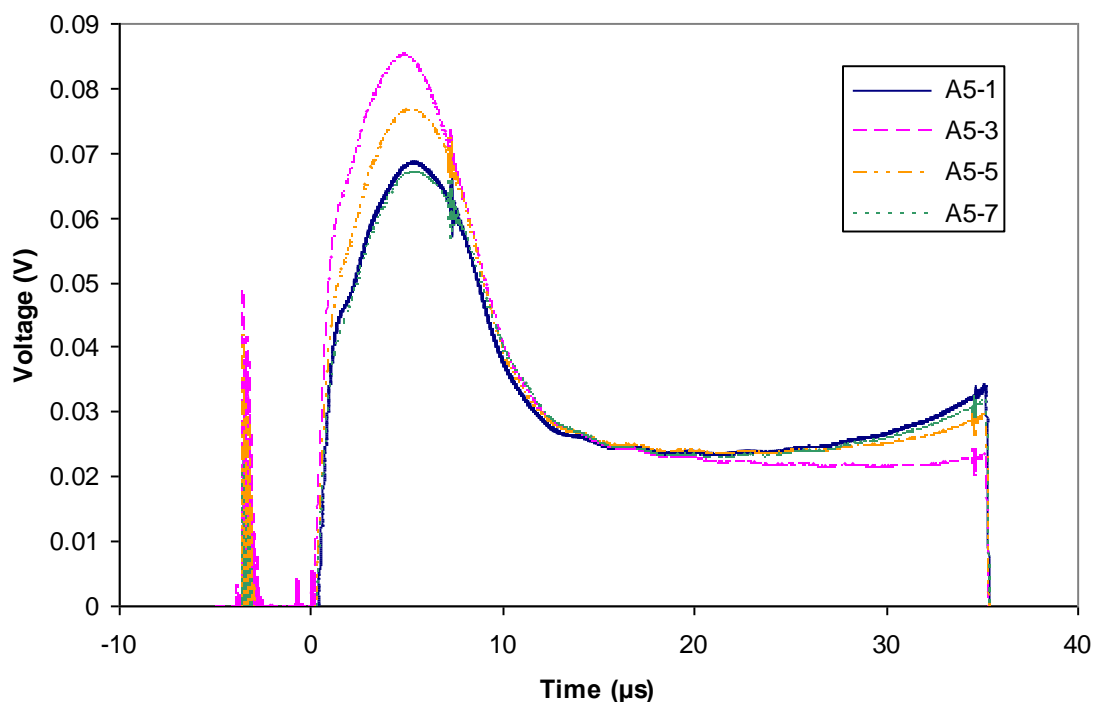
The general shape of Figure 16 is evident in these experimental results. Transit time can be extracted from the time of the maximum extraction current.

The time between application of the light pulse and the maximum of the curve below is 4.59 μs. This leads to a mobility value of  $\mu = 2.03 \times 10^{-5} \text{ cm}^2/\text{Vs}$ . Results from many different samples all gave values ranging from 1 to  $3 \times 10^{-5} \text{ cm}^2/\text{Vs}$ . Five such sample measurements are presented in Table 7.

**Table 7: Photo-CELIV – mobility values**

Sample	$\mu(\text{cm}^2/\text{Vs})$
G1.5	$1.19 \times 10^{-5}$
G1.6	$1.46 \times 10^{-5}$
G1.8	$1.18 \times 10^{-5}$
G4.3	$1.87 \times 10^{-5}$
G4.6	$2.03 \times 10^{-5}$

As mentioned previously, we also collaborated with members of Dr. Asbury's group in the Chemistry department who have approximately one year of expertise in making CELIV measurements. The resulting voltage traces are shown in Figure 26.

**Figure 26: CELIV – voltage signals from samples tested at Asbury lab**

Four different samples were tested, all with similar transit times. Interestingly, the order the samples were tested is from highest peak to lowest peak. This raises questions as to if the samples were degrading slightly during the measurement, which exposed the samples to air for several hours and intense laser radiation for several minutes.

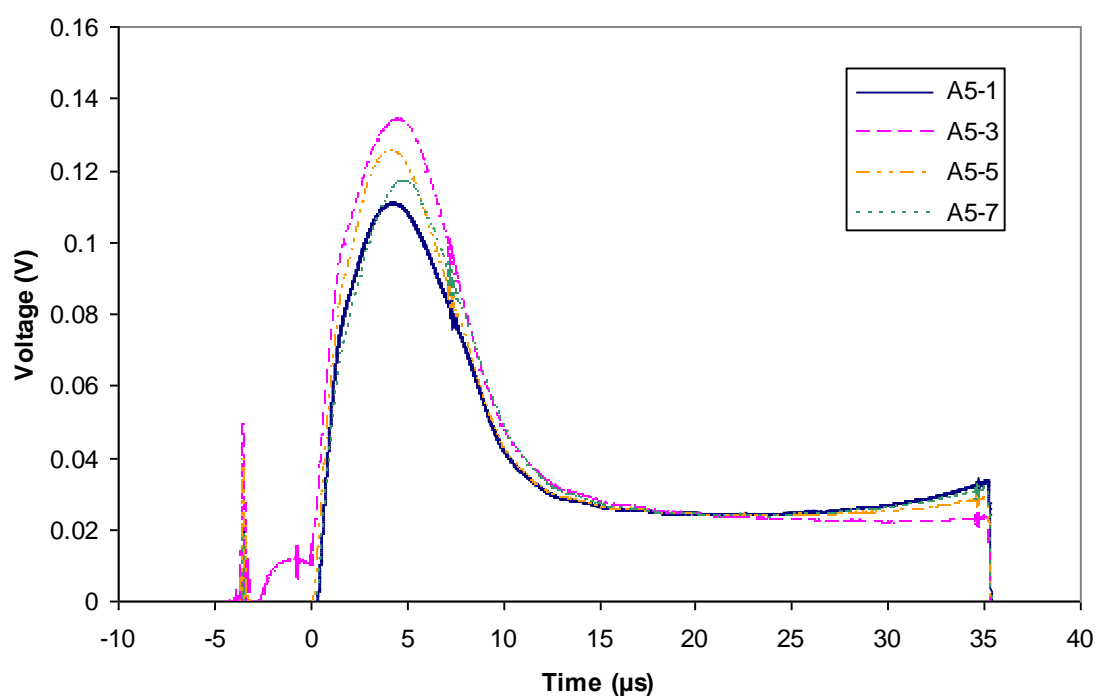
The mobility values resulting from these voltage traces are given in Table 8.



**Table 8: CELIV – mobility values from samples tested at Asbury lab**

Sample	$\mu(\text{cm}^2/\text{Vs})$
A5-1	$1.73 \times 10^{-5}$
A5-3	$1.73 \times 10^{-5}$
A5-5	$1.68 \times 10^{-5}$
A5-7	$1.86 \times 10^{-5}$

Photo-CELIV studies were also performed at the Asbury lab with very similar results, albeit a slightly wider range in values was obtained.

**Figure 27: Photo-CELIV – voltage signals from samples tested at Asbury lab**

The same four samples were tested under illumination. A wider distribution of transit times led to more variation in the mobility results.

**Table 9: Photo-CELIV – mobility values from samples tested at Asbury lab**

Sample	$\mu(\text{cm}^2/\text{Vs})$
A5-1	$2.15 \times 10^{-5}$
A5-3	$1.58 \times 10^{-5}$
A5-5	$2.00 \times 10^{-5}$
A5-7	$1.47 \times 10^{-5}$

## Chapter 6

### Discussion

It is paramount to compare results to accepted literature values in order to help judge the validity of the measurements. With that in mind, the following figure plots electron mobility values for P3HT-PCBM calculated by several different groups, including three representative data points from our I-TOF experiments. The range of values we measured in our experiments was within the accepted range of values already published in literature.

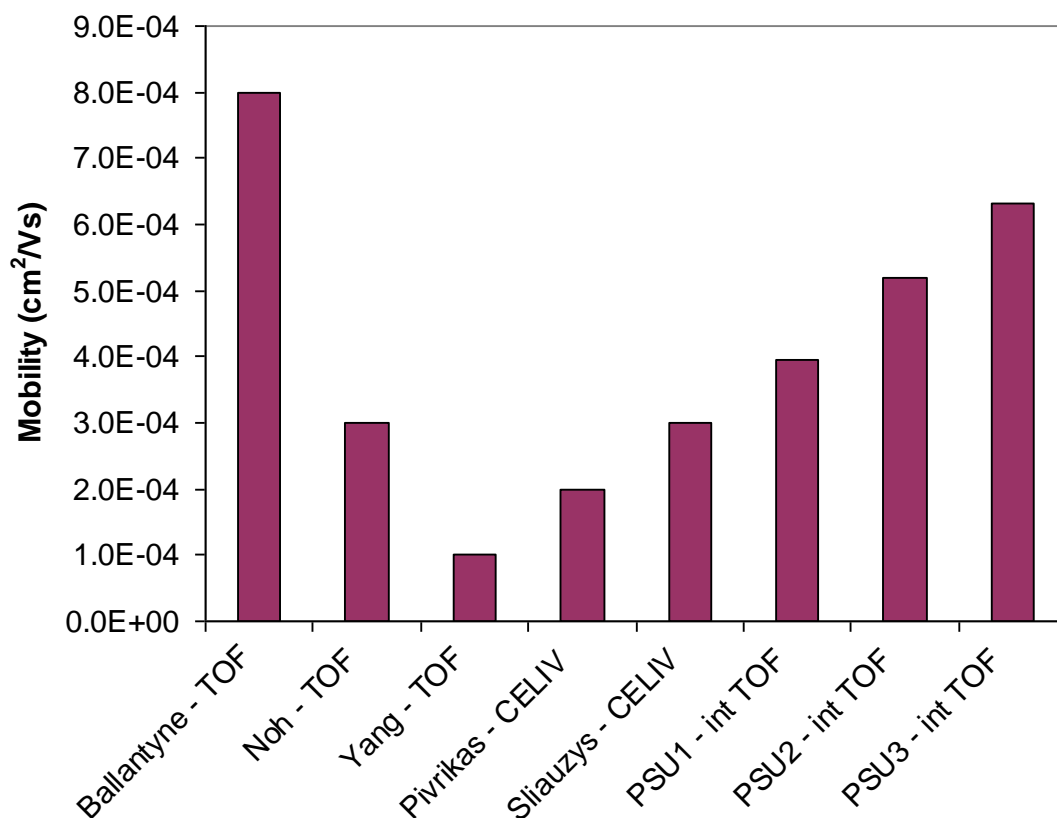


**Figure 28: Comparison of P3HT:PCBM mobility results to accepted literature values**

Our electron mobility values fell in line with what has been reported in the literature for P3HT:PCBM.

### 6.1. Capacitance independence of mobility

As shown in Table 6, the value of capacitance used to collect charges in the integral TOF experiment did not affect the value of the mobility measured. What this proves is that it does not matter which capacitance we use for the experiment. The role of the capacitor is simply to collect the fast charges arriving from the device due to the light pulse. The only change when swapping capacitors is that the time it takes to decay back to the initial equilibrium state is changed. Therefore, the only requirement is to choose a capacitor that allows the signal to decay fast enough, where “fast enough” is judged based on the repetition rate of the laser source.

### 6.2. Negative voltage dependence of mobility

Normally, it is expected that an increased voltage should increase mobility, due to an increased electric field and therefore a tendency toward faster drift velocity. However, this is not always the case for polymer-based samples, as shown in the literature. Several groups have observed a negative mobility dependence on electric field at room temperature; only at reduced temperatures do they observe the expected positive correlation [6, 40]. These trends are typically plotted on a semi-log scale to show that  $\log \mu \propto \sqrt{E}$ , which is the Poole-Frenkel relationship.

Recalling Figure 23, this is exactly what we saw for our samples. Validating this observation is important, but it is difficult to explain why this happens. Kažukauskas offers a physical explanation as to why this negative dependence at low electric fields is seen by evaluating the material in a Gaussian disorder model [6]. Essentially, in this model, hopping transport occurs between sites with a Gaussian distribution of energy. Different energy at different localized states is due to fluctuation in conjugation lengths and structural disorder. By conducting Monte Carlo simulations of hopping through a material with energetic and positional

disorder, Kažukauskas showed that the negative dependence occurs when the spatial disorder exceeds the energetic disorder. This leads him to believe that the carriers may be able to find more energetically favorable paths by taking a more sinuous route at the lowest electric fields. When the field is increased, the carriers are forced to move in a given direction, which may not be the most energetically favorable due to the spatial disorder. In theory, this would decrease the mobility until very high electric fields are reached, in which case there is enough energy to make up for these spatial disorder barriers. At the current time, this theory may be the best explanation available for the negative dependence of mobility on the electric field seen in these polymer-based solar cells.

### **6.3. Intensity dependence of mobility**

At higher intensities, there was little to no change in the mobility value measured. This is shown in Figure 24. The laser intensity should not affect the measured mobility unless there is a problem with the experiment. Problems that might occur could be related to some sort of dynamical effects caused by the very high peak power of the femtosecond laser. Thermal energy generated by the pulse could cause some unforeseen effects. Also, there is always the possibility of photobleaching playing a higher role at high intensity. It is true that we witnessed some degradation of the samples over time after they were used for many tests, but this was not studied in depth. Finally, the mobility may vary with intensity if not all the charges built up on the surface are being injected through the sample. This situation would invalidate the measurement, since the I-TOF derivation given in Section 2.2.2 assumes that all surface charge is injected. With this in mind, Figure 24 shows the data taken with the laser diode is a lower value than for the femtosecond laser. For this reason, the data taken with the laser diode is believed to be

underestimated compared to the femtosecond laser data. Therefore, the results section of this paper contains data collected using the femtosecond laser.

#### 6.4. Comparison of I-TOF and CELIV

For our work, the integral mode TOF measurements typically gave values an order of magnitude higher than the CELIV measurements. Several factors could be influencing this. First, CELIV was initially developed to overcome limitations of the I-TOF measurement for highly conductive samples [7]. Specifically, in samples with a high conductivity such as P3HT:PCBM, the dielectric relaxation time  $\tau_\sigma$  will be relatively short. If it is not much larger than the small signal transit time,  $t_{tr}$ , then the electric field may be redistributed in the sample, violating the assumption of a homogeneous electric field. As suggested by Juška, one must use a pulsed laser source and decrease the delay time between the voltage and laser pulses if this problem occurs. The necessity of this solution is illustrated in Figure 29, where it is shown that the collected charge is underestimated when the delay time is too long.

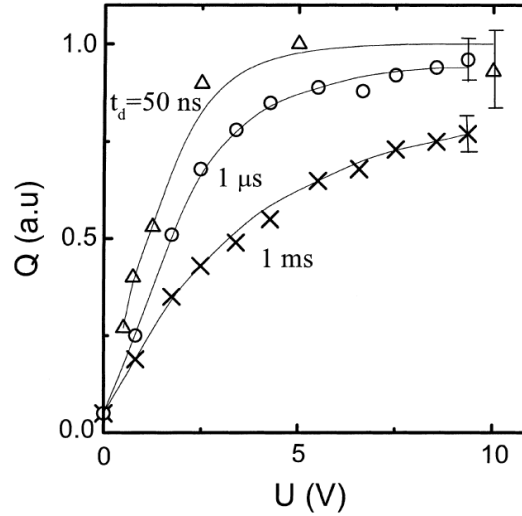


**Figure 29: Collected charge vs. applied voltage for  $\mu$ c-Si:H**

A short delay time between voltage and laser pulses is necessary, or the collected charge and transit distance will be underestimated, resulting in an overestimated mobility value.

Unfortunately, attempting to close this gap poses another problem. The application of the voltage pulse causes a displacement current in the device and the collection capacitor. The timescale for this displacement current to “turn on” is long in our devices, close to 1  $\mu\text{s}$ . If attempting to move the laser pulse any closer to the front of the voltage pulse, the extraction will occur while the displacement current is still reaching its steady state value. This will cause the two effects to interfere with each other, and deconvoluting the extraction signal from the displacement current will prove impossible. In order to get an analyzable signal, we had to keep the delay in our experiments around 1  $\mu\text{s}$ . This may cause our I-TOF results to be slightly overestimated, due to the electric field redistributing and concentrating near the edges, causing transport over a distance shorter than the full thickness.

Another potential factor is that the measured lifetime of the charge carriers is not much longer than the transit time of the initial carrier front. A typical  $\mu\tau$ -product measured from the plateau voltage of an I-TOF test might yield a value of  $3 \times 10^{-15} \text{ m}^2/\text{V}$ , which corresponds to a lifetime of just  $\tau = 53 \text{ ns}$ . Given that the transit time is often in the neighborhood of  $t_{\text{tr}} = 40 \text{ ns}$ , some significant trapping may occur during the transit, and part of the signal could be lost. This could compound the problem created by a quick dielectric relaxation time, and it may help to explain the discrepancy between I-TOF and CELIV results.

One positive comparison that can be made is the similarity in results between the CELIV measurements done at the laser center and in the Asbury lab. The results corroborate each other and build confidence in CELIV as a more accurate alternative for I-TOF.

Nonetheless, we must also consider the limitation of CELIV in that it is difficult to separately measure electrons and holes. Initially, the CELIV measurement itself is designed to extract equilibrium carriers. Most materials have an abundance of either electrons or holes, limiting CELIV to the measurement of majority carrier mobility. In photo-CELIV, both electrons and holes are photogenerated. However, only one peak is seen. As mentioned in the literature

review, this indicates that electrons and holes have nearly the same mobility, and therefore the measured mobility is a blend between the two [40]. This is evidenced in the CELIV curves we have taken (Figures 25-27). Only one peak is clearly distinguishable. However, upon close inspection, a slight shoulder can be seen on the rising edge of some of these peaks. This indicates that either electrons or holes may be slightly faster than their counterpart.

Because the two peaks cannot be accurately deconvoluted, additional measures must be taken to determine which are the faster carriers. First, light must be strongly absorbed near the surface of the sample. This involves choosing a wavelength of light that is strongly absorbed by the sample and also ensuring that the sample is thick compared to its absorption depth. Then, the carriers generated near the surface are subjected to the linearly increasing voltage. One type of carrier will have to travel the entire thickness of the sample, while the other carrier will be extracted immediately as it is near the surface. This is the way to determine which carrier has the faster transit. For now, we are only able to report one mobility value for both electrons and holes, assured that both carriers are near the same value.

## **Chapter 7**

### **Conclusions**

#### **7.1. Summary of accomplished work**

Integral mode time-of-flight, CELIV, and photo-CELIV measurements have been performed on P3HT:PCBM solar cell samples. A complete experimental setup capable of all three types of measurements has been constructed, including all necessary optics and electronics.

Mobility has been calculated for all of these tests. Because of the nature of the P3HT:PCBM devices, the electrons and holes have nearly balanced mobilities, so the value calculated should be valid for both. This assumption is supported by the shape of the CELIV curves. Only one peak is distinguishable, so the transit times and mobilities for electrons and holes must be quite similar, at least within about a factor of 4. Using the integral time of flight method, the  $\mu\tau$ -product was also calculated so that trapping could be studied.

Overall, two effective methods for studying charge transport and determining mobility for thin film organic solar cell devices have been tested. These methods give complementary data, and thus they can be used in conjunction with one another for future studies of other hybrid solar cells.

#### **7.2. Description of future work**

Many future tweaks and enhancements can be made to improve results. First, the Asbury lab is accustomed to using silver paint as an adhesive on top of the Al electrode. A gold wire is placed in the silver paint while wet and allowed to dry until a reasonably strong contact is made. The other end of the gold wire has a ball of indium clamped and/or soldered to it. This provides a



better contact for the clip which connects to it. Usually this connection is much more stable than the copper wire spring approach. However, when we tried this method, the silver paint tended to spill over our Al contacts, shorting the devices. In the future, if we fabricate some devices as large as Asbury's lab usually does, we may be able to utilize this silver paint technique. The main problem with using the copper wire is that it gets disturbed by the vacuum easily and contact is lost. It is likely that use of the silver paint would eliminate this problem.

Additionally, a permanent measurement station for the TOF measurement can be created. This would simplify the experiment to a "black box," with connections for voltage input, signal input and oscilloscope output on the outside. Soldering the resistor, capacitor, and wiring together inside a box like this with only BNC connections leading out might help to eliminate excess noise in the signal, producing a cleaner measurement. At the least, it will make the experiment easier for the next person to undertake it.

Continuing work on the CELIV measurements may yield further information about trapping in our samples. By varying the delay time between laser pulse and voltage ramp, fewer and fewer carriers are available to be extracted as recombination and trapping occur. Studying the change in signal as delay time increases can give valuable information on the rates of these processes. This is actually the reason Asbury's lab became interested in CELIV – because their specialty is in spectroscopy and kinetics-related matters.

Lastly, there is much more work to be done in probing the mobility of hybrid polymer-nanocrystal solar cell devices. Some initial results have been obtained, but they are too immature to include with the rest of this thesis. This new field requires a great deal of work to attain performance similar to polymer/fullerene samples, which have been studied and improved for years. This thesis has developed and compared two reliable techniques for characterizing carrier transport in this class of materials. From this stepping stone, we can begin to improve our devices by identifying which fabrication techniques produce the highest mobility cells.

## References

- [1] J. Huang, G. Li, Y. Yang, *App. Phys. Lett.* 87, 112105 (2005)
- [2] S. Noh, J. Kim, C. Lee, M. Lee b, B. Jung, D. Hwang, S. Lee, H. Kim, *Proc. of SPIE* 6334, 63340S (2006)
- [3] A. M. Ballantyne, L. Chen, J. Dane, T. Hammant, F. M. Braun, M. Heeney, W. Duffy, I. McCulloch, D. D. C. Bradley, J. Nelson, *Adv. Funct. Mater.* 18, 2373–2380 (2008)
- [4] A. Pivrikas, N. S. Sariciftci, G. Juška, and R. Österbacka, *Prog. Photovolt: Res. Appl.* 15, 677–696 (2007)
- [5] G. Sliaužys, G. Juška, K. Arlauskas, A. Pivrikas, R. Österbacka, M. Scharber, A. Mozer, N. S. Sariciftci, *Thin Solid Films* 511–512, 224–227 (2006)
- [6] V. Kažukauskas, M. Pranaitis, V. Čyras, L. Sicot, F. Kajzar, *Eur. Phys. J. Appl. Phys.* 37, 247–251 (2007)
- [7] G. Juška, K. Arlauskas, M. Viliunas, J. Kočka, *Phys. Rev. Lett.* 84, 4946-4949 (2000)
- [8] R. C. Paddock, Oil giant primes the biofuel pump with \$500 million, *L.A. Times*, Los Angeles, Calif.: Feb 2, 2007. pg. B.1
- [9] A. L. Wadell, S. R. Forrest, *Green Power*, 1-2 (2006)
- [10] J. Reynolds, Solar panels in clothing could keep us talking, *The Scotsman*, Dec 16, 2004, <<http://thescotsman.scotsman.com/index.cfm?id=1433222004>>
- [11] W. Ma, C. Yang, X. Gong, K. Lee, A. J. Heeger, *Adv. Funct. Mater.* 15, 1617-1622 (2005)
- [12] Z. Hens, E. S. Kooij, G. Allan, B. Grandidier, D. Vanmaekelbergh, *Nanotechnology* 16, 339–343 (2005)
- [13] V. I. Klimov, *App. Phys. Lett.* 89, 123118 (2006)
- [14] P. Weiss, *Science News* 169, 344 (2006)
- [15] Kronholm, D, Hummelen, J. C., *SPIE Newsroom*, October 2008, DOI: 10.1117/2.1200810.1232
- [16] R. D. Schaller, V. I. Klimov, *Phys. Rev. Lett.* 92, 186601 (2004)
- [17] X. Jiang, S. B. Lee, I. B. Altfeder, A. A. Zakhidov, R. D. Schaller, J. M. Pietryga, V. I. Klimov, *Proc. of SPIE* 5938, 59381F (2005)

- [18] X. Jiang, R. D. Schaller, S. B. Lee, J. M. Pietryga, V. I. Klimov, A. A. Zakhidov, J. Mater. Res., 22, 2204–2210 (2007)
- [19] S. Günes, K. P. Fritz, H. Neugebauer, N. S. Sariciftci, S. Kumar, G. D. Scholes, Solar Energy Materials & Solar Cells 91, 420–423 (2007)
- [20] W. J. E. Beek, M. M. Wienk, R. A. J. Janssen, Adv. Funct. Mater. 16, 1112–1116 (2006)
- [21] C. E. Finlayson, D. S. Ginger, E. Marx, N. C. Greenham, Phil. Trans. R. Soc. Lond. A 361, 363–377 (2003)
- [22] J. Zhu, H. Peng, C. K. Chan, K. Jarausch, X. F. Zhang, Y. Cui, Nano Lett. 7, 1095–1099 (2007)
- [23] L. Wang, Y. Liu, X. Jiang, D. Qin, Y. Cao, J. Phys. Chem. C, 111, 9538–9542 (2007).
- [24] J. Boucle, S. Chyla, M. S. P. Shaffer, J. R. Durrant, D. D. C. Bradley, J. Nelson, Adv. Funct. Mater. 18, 622–633 (2008)
- [25] Y. Zhou, Y. Li, H. Zhong, J. Hou, Y. Ding, C. Yang, Y. Li, Nanotechnology 17, 4041–4047 (2006)
- [26] I. Gur, N. A. Fromer, C. Chen, A. G. Kanaras, A. P. Alivisatos, Nano Lett. 7, 409–414 (2007)
- [27] K. S. Leschkies, R. Divakar, J. Basu, E. Enache-Pommer, J. E. Boercker, C. B. Carter, U. R. Kortshagen, D. J. Norris, E. S. Aydil, Nano Lett. 7, 1793–1798, (2007)
- [28] H. Lee, S. W. Yoon, E. J. Kim, J. Park, Nano Lett. 7, 778–784 (2007)
- [29] J. Kočka, G. Juška, O. Klíma, E. Šípek, G. Nobile, E. Terzini, G. Conte, J. Non-Cryst. Solids 164–166, 489–492 (1993)
- [30] A. Carbone, B. K. Kotowska, D. Kotowski, Phys. Rev. Lett. 95, 236601 (2005)
- [31] K. Genevičius, R. Österbacka, G. Juška, K. Arlauskas, H. Stubb, Synth. Metals 137, 1407–1408 (2003)
- [32] G. Juška, K. Genevičius, M. Viliunas, K. Arlauskas, H. Stuchlíková, A. Fejfar, J. Kočka, J. Non-Cryst. Solids 266–269, 331–335 (2000)
- [33] W.E.Spear, *Amorphous Silicon and Rel.Mat.* ed. H.Fritzsche, World Scientific, Singapore, 721–765 (1988)
- [34] G. Juška, G. Jukonis, J. Kočka, J. Non-Cryst. Solids 114, 354–356 (1989)
- [35] K. K. Kanazawa, I. P. Batra, J. Appl. Phys. 43, 1845–1853 (1972)

- [36] I. P. Batra, K. K. Kanazawa, B. H. Schechtman, H. Seki, *J. Appl. Phys.* 42, 1124-1130 (1971)
- [37] R. Österbacka, G. Juška, K. Arlauskas, H. Stubb, *Proc. of SPIE* 3145, 389-394 (1997)
- [38] A. Pivrikas, G. Juška, K. Arlauskas, M. Scharber, A. Mozer, N.S. Sariciftci, H. Stubb, R. Österbacka, *Proc. of SPIE* 5938, 59380N (2005)
- [39] G. Juška, K. Arlauskas, R. Österbacka, H. Stubb, *Synth. Metals* 109, 173–176 (2000)
- [40] A. J. Mozer, G. Dennler, N.S. Sariciftci, M. Westerling, A. Pivrikas, R. Österbacka, G. Juška, *Phys. Rev. B* 72, 035217 (2005)
- [41] A. J. Mozer, N.S. Sariciftci, A. Pivrikas, R. Österbacka, G. Juška, L. Brassat, H. Bässler, *Phys. Rev. B* 71, 035214 (2005)
- [42] V. D. Mihailetschi, H. Xie, B. de Boer, L. J. A. Koster, P. W. M. Blom, *Adv. Funct. Mater.* 16, 699-708 (2006)
- [43] C. Waldauf, P. Schilinsky, J. Hauch, C. J. Brabec, *Thin Solid Films* 451–452, 503–507 (2004)